

SN 2020ank – a bright and fast-evolving H-deficient superluminous supernova

Amit Kumar^{1,2★}, Brajesh Kumar^{1,3}, S. B. Pandey^{1†}, D. K. Sahu³, Avinash Singh^{1,3}, G. C. Anupama³, Amar Aryan^{1,4}, Rahul Gupta^{1,4}, Anirban Dutta³ and Kuntal Misra¹

¹Aryabhata Research Institute of Observational Sciences, Manora Peak, Nainital 263 002, India

²School of Studies in Physics and Astrophysics, Pandit Ravishankar Shukla University, Chattisgarh 492 010, India

³Indian Institute of Astrophysics, II Block, Koramangala, Bengaluru 560 034, India

⁴Department of Physics, Deen Dayal Upadhyaya Gorakhpur University, Gorakhpur 273 009, India

Accepted XXX. Received 2020; in original form ZZZ

ABSTRACT

We investigate the observational properties of a hydrogen-deficient superluminous supernova (SLSN) SN 2020ank (at $z = 0.2485$), with the help of early phase observations carried out between -21 to $+52$ d since g -band maximum. Photometrically, SN 2020ank is one of the brightest SLSN ($M_{g,peak} \sim -21.84 \pm 0.10$ mag), having fast pre-peak rising and post-peak decaying rates. The bolometric light-curve of SN 2020ank exhibits a higher peak luminosity (L_{max}) of $\sim (3.9 \pm 0.7) \times 10^{44}$ erg s⁻¹ and appears to be symmetric around the peak with $L_{max}^{rise}/e \approx L_{max}^{fall}/e \approx 15$ d. The semi-analytical light-curve modelling using the MINIM code suggests a spin down millisecond magnetar with $P_i \sim 2.2 \pm 0.5$ ms and $B \sim (2.9 \pm 0.1) \times 10^{14}$ G as a possible powering source for SN 2020ank. The possible magnetar origin and excess ultra-violet flux at early epochs indicate a central-engine based powering source for SN 2020ank. Near-peak spectra of SN 2020ank are enriched with the W-shaped O II features but with the weaker signatures of C II and Fe III. Using the estimated rise time of ~ 27.9 d and the photospheric velocity of $\sim 12,050$ km s⁻¹, we constrain the ejecta mass to $\sim 7.2 M_{\odot}$ and the kinetic energy of $\sim 6.3 \times 10^{51}$ erg. The near-peak spectrum of SN 2020ank exhibits a close spectral resemblance with that of fast-evolving SN 2010gx. The absorption features of SN 2020ank are blue-shifted compared to Gaia16apd, suggesting a higher expansion velocity. The spectral similarity with SN 2010gx and comparatively faster spectral evolution than PTF12dam (a slow-evolving SLSN) indicate the fast-evolving behavior of SN 2020ank.

Key words: techniques: photometric – techniques: spectroscopic – supernovae: general – supernovae: individual (SN 2020ank)

1 INTRODUCTION

Superluminous supernovae (SLSNe) are nearly 2–3 magnitudes brighter than classical SNe (Angus et al. 2019; Gal-Yam 2019a; Inserra 2019) radiating total energy in the order of $\sim 10^{51}$ erg and exhibit characteristic W-shaped O II features towards blue in the near-peak spectra (Quimby et al. 2011, 2018; Gal-Yam 2019b). SLSNe are rare class of events with high-peak luminosity and were unknown before SN 2005ap (Quimby et al. 2007). They comprise $\sim 0.01\%$ of normal core-collapse SNe (CCSNe), and nearly 150 objects have been spectroscopically confirmed so far (Quimby et al. 2013; McCrum et al. 2015; Liu et al. 2017b; Prajs et al. 2017; Gomez et al. 2020). Based on the Hydrogen abundance,

these events are broadly classified into H-poor SLSNe (SLSNe I) and H-rich SLSNe (SLSNe II) (Gal-Yam 2012; Branch & Wheeler 2017). Most of the SLSNe I generally occur in metal-poor faint dwarf galaxies (Lunnan et al. 2014; Chen et al. 2017a) with complex light-curves having pre-peak bumps (e.g., LSQ14bdq; Nicholl et al. 2015b, see also Angus et al. 2019) and post-peak undulations (e.g., SN 2015bn; Nicholl et al. 2016). On the other hand, SLSNe II mostly present prominent and narrow hydrogen Balmer lines, also characterised as SLSNe IIn due to their spectral similarity with lower luminosity SNe IIn (e.g., SN 2008am; Chatzopoulos et al. 2011). However, some of these events lack the typical narrow hydrogen features, e.g., SN 2008es (Gezari et al. 2009; Miller et al. 2009), SN 2013hx and PS15br (Inserra et al. 2018a). SLSNe IIn have primarily been found in heterogeneous host environments and remain less-studied (Leloudas et al. 2015; Perley et al. 2016; Schulze et al. 2018).

★ E-mail: amit@aries.res.in

† E-mail: shashi@aries.res.in

SLSNe I appear to have slow- and fast-evolving behaviour based on their different photometric and spectroscopic properties (Inserra et al. 2017; Vreeswijk et al. 2017; Quimby et al. 2018; Pursiainen et al. 2018; Inserra et al. 2018c; Inserra 2019; Könyves-Tóth & Vinkó 2020). Photometrically slow-evolving (“PTF12dam-like”; rise time ~ 33 –100 d) SLSNe I also exhibit slower spectroscopic evolution in comparison to the fast-evolving (“SN 2011ke-like”; rise time ~ 13 –35 d) SLSNe I (Quimby et al. 2018). In addition, the slow-evolving SLSNe I have lower SN expansion velocity (v_{exp}) of $\lesssim 12,000 \text{ km s}^{-1}$ and shallower velocity gradient (between 10 to 30 d, post-peak), whereas fast-evolving ones show comparatively higher v_{exp} of $\gtrsim 12,000 \text{ km s}^{-1}$ and steeper velocity gradient in the same time regime (Inserra et al. 2018a).

The physical mechanism giving rise to the high peak-luminosity feature in most of the SLSNe I remains debatable. The widely accepted physical mechanism of radioactive decay (RD) of ^{56}Ni for normal class of H-deficient CCSNe has been found to be inefficient in explaining the observed high peak-luminosity in most of the SLSNe I. Theoretically, this would require a higher nickel mass (M_{Ni}) synthesis ($\gtrsim 5 M_{\odot}$; Gal-Yam 2012), generally not possible in the core-collapse system (Umeda & Nomoto 2002, 2008). An alternate theory based on pair-instability SNe (PISNe; Kozyreva & Blinnikov 2015) has been considered to explain features in some of the slow-evolving SLSNe I (e.g., SN 2007bi; Gal-Yam et al. 2009). However, the sharper pre-peak rising rates and bluer colours of these objects are not favorable with this scenario (Kasen et al. 2011; Dessart et al. 2012; Jerkstrand et al. 2017). Various other plausible models are also proposed to explain the relatively wider and luminous bolometric light-curves of these Ultra-Violet (UV) bright cosmic events, including Circumstellar Matter Interaction (CSMI; Ginzburg & Balberg 2012; Wheeler et al. 2017), Spin-down Millisecond Magnetar (MAG; Kasen & Bildsten 2010; Woosley 2010; Metzger et al. 2015; Chen et al. 2017b; Dessart 2019), and their possible combinations, termed as “HYBRID” (Chatzopoulos et al. 2012) models, e.g., CSMI+RD, CSMI+MAG, CSMI+RD+MAG (Chatzopoulos et al. 2013; Moriya et al. 2018; Chatzopoulos & Tuminello 2019; Wang et al. 2019).

Detailed studies for individual SLSNe I reveal that no single model is sufficient to explain all observed phenomena in these systems. For example, a handful of SLSNe I (iPTF13ehe; Yan et al. 2015, iPTF15esb and iPTF16bad; Yan et al. 2017b) manifest clear spectral signatures supporting the CSMI. The shock-cooling of the extended CSM usually explains the observed pre-peak bumps in the light-curves of SLSNe I (e.g., SN 2006oz; Leloudas et al. 2012, DES14X3taz; Smith et al. 2016), see also Piro (2015). Whereas, ejecta interaction with the pre-expelled CSM shells is considered as the potential reason for the post-peak undulations (e.g., SN 2007bi; Gal-Yam et al. 2009, SN 2015bn; Nicholl et al. 2016), favoring the CSMI. On the other hand, there are a few observational features which favor the MAG model. For instance, the near-peak excess UV flux in the case of Gaia16apd (Nicholl et al. 2017a) is explained in terms of a central engine based power source: it may be a spin-down millisecond magnetar or a mass accreting black-hole (MacFadyen & Woosley 1999). Similarly, SLSN 2011kl, the only known case so far associated with the ultra-long Gamma-Ray Burst (UL-GRB), e.g., GRB 111209A (Greiner et al. 2015), also supports the central engine based powering mechanism (Bersten et al. 2016; Lin et al. 2020) and hints that some of these SLSNe I may also be connected with long GRBs (Kann et al. 2019). We note that both the models (CSMI and MAG) can explain various observational aspects in the SLSNe I light curves (Inserra et al. 2013; Nicholl et al. 2014), though a few specific features favour

the MAG model, including the near-peak high UV flux (Mazzali et al. 2016; Nicholl et al. 2017a), late-time flattening (Inserra et al. 2013; Liu et al. 2017a; Nicholl et al. 2017b; Blanchard et al. 2018) and spectral properties (Dessart et al. 2012; Nicholl et al. 2019). Though, deeper investigations are required to explore the underlying physical mechanisms, possible progenitors and environments hosting such rare and energetic explosions.

SN 2020ank (ZTF20aahbfmf) was discovered by the Zwicky Transient Facility (ZTF; Bellm et al. 2019) on 2020 January 19 at J2000 coordinates: RA = $08^{\text{h}}16^{\text{m}}14^{\text{s}}.65$ and Dec = $+04^{\circ}19'26''.87$ (Poidevin et al. 2020a). SN 2020ank was also detected by the Asteroid Terrestrial-impact Last Alert System (ATLAS; Denneau 2014) with internal name ATLAS20dzt on 2020 January 24 (Tonry et al. 2020) and by the Pan-STARRS1 (PS1; Chornock et al. 2013) on 2020 March 18 as PS20eyd. SN 2020ank was classified as a SLSN I based on the spectroscopic observations from the Liverpool Telescope (LT-2.0m) and the Gran Telescopio Canarias (GTC-10.4m; Poidevin et al. 2020b). Later on, spectroscopic observations were also carried out by Dahiwalé & Fremling (2020), discussing the spectrum obtained from the Palomar Observatory Hale Telescope (P200-5.1m) reporting redshift $z = 0.2485$. The near-peak polarimetric observations showing negligible polarization, as investigated by Lee (2020), suggests a nearly spherical explosion for SN 2020ank.

In this paper, early time photometric and spectroscopic observations of SN 2020ank have been discussed. The paper is structured as follows. The procedures describing observations, data reductions, and analysis are explained in section 2. In section 3, the photometric properties of SN 2020ank and its comparison with other well studied SLSNe I are presented. The bolometric light-curve modelling using the MINIM code is presented in section 4. Section 5 describes the spectroscopic properties of SN 2020ank, the SYNAPPS spectral modelling, and the spectral comparison with other well studied SLSNe I. We conclude our results in Section 6. Throughout this work, $H_0 = 70 \text{ km s}^{-1} \text{ Mpc}^{-1}$ and $\Omega_m = 0.27$ have been adopted to estimate the distances, dates are presented in UT, and phase is given since g -band maximum.

2 OBSERVATIONS AND DATA ANALYSIS

Photometric observations in Bessell U , B , V , R , and I bands of SN 2020ank field were carried out with three ground-based observing facilities in India: Sampurnanand Telescope (ST-1.04m), Himalayan Chandra Telescope (HCT-2.0m), and recently commissioned Devasthal Optical Telescope (DOT-3.6m) having longitudinal advantage for time critical observations (Pandey 2016, 2018). These three telescopes are equipped with liquid nitrogen cooled CCD cameras at their Cassegrain focus. The observations were initiated using the ST-1.04m and continued with the HCT-2.0m (4 epochs) and DOT-3.6m (6 epochs). Photometric images were acquired with the $4\text{K} \times 4\text{K}$ CCD Imagers mounted at the axial ports of both the ST-1.04m and the DOT-3.6m (Pandey et al. 2018). In addition, the Himalayan Faint Object Spectrograph and Camera (HFOSC¹) instrument at the HCT-2.0m has also been used to perform the multi-band photometric data of SN 2020ank. Table 1 lists various parameters of the facilities and their back-end instruments. Standard IRAF² tasks were executed to pre-process (e.g., bias-subtraction, flat-fielding and cosmic ray removal) the raw data. On

¹ https://www.iiap.res.in/?q=iao_about

² <http://iraf.noao.edu/>

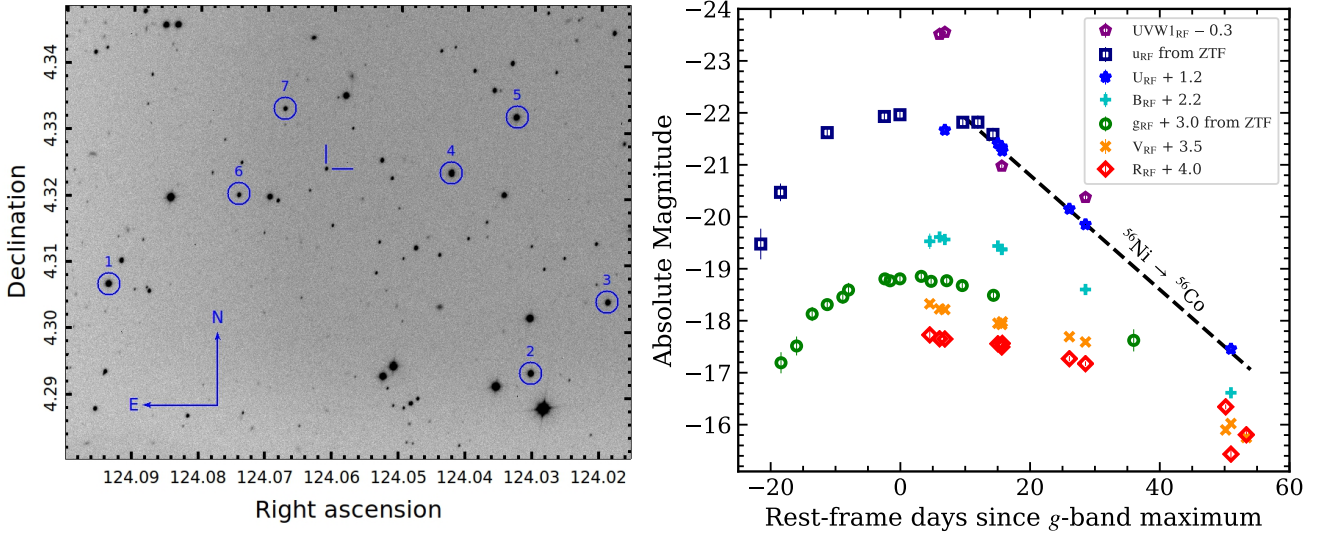


Figure 1. *Left:* Finding chart of SN 2020ank ($\sim 5' \times 4'$ field) along with other local standard stars (marked in circles, IDs 1–7). The R -band image (exposure time = 5 min) observed on 2020 March 19 using the $4K \times 4K$ CCD Imager mounted at the axial port of the DOT-3.6m. The location of SN is marked with a blue crosshair. North and East directions are also indicated in the image. *Right:* The temporal evolution of SN 2020ank in $UVW1_{RF}$, u_{RF} , U_{RF} , B_{RF} , g_{RF} , V_{RF} , and R_{RF} bands. The light curves are corrected for the Galactic extinction and the K -corrections are applied using our spectral analysis. The post-peak decay rate of U_{RF} light curve is well in agreement with the decay rate of $^{56}\text{Ni} \rightarrow ^{56}\text{Co}$ theoretical curve (0.11 mag d^{-1}).

several nights, multiple science frames in each band were stacked after the alignment of the individual images, and consequently, a better signal-to-noise ratio was obtained. To calibrate a sequence of secondary standards in the SN field, we observed Landolt photometric standard fields PG 1657 and PG 0231 (Landolt 1992). The standard and SN fields were observed on 2020 March 19 (PG 1657) and 2020 October 14 (PG 0231) with the DOT-3.6m under good photometric conditions. The Landolt field stars have a brightness range of $12.77 \leq V \leq 16.11 \text{ mag}$ and colour range of $-0.15 \leq B - V \leq 1.45 \text{ mag}$. Using the stand-alone version of DAOPHOT³ (Stetson 1987, 1992), the point spread function photometry on all the frames was performed. The average atmospheric extinction values in U , B , V , R , and I bands for the Devasthal site were adopted from Mohan et al. (1999). Using the Landolt standards, transformation to the standard system was derived by applying average colour terms, and photometric zero-points. In the left panel of Figure 1, the seven secondary calibrated standard stars (used to calibrate the SN magnitudes) are marked, and the respective U , B , V , R , and I magnitudes are listed in Table 2. The final SN photometry in U , B , V , R , and I bands are listed in Table 3. Here we note that for completeness, in addition to our observations, the publicly available ZTF g and r bands data are also used (Poidevin et al. 2020a) and downloaded from the Lasair⁴ website (Smith et al. 2019).

The optical spectroscopic observations of SN 2020ank in low-resolution mode were performed at four epochs from HCT-2.0m using the HFOC instrument. The spectra were obtained using grism-Gr7 (3500–7800 Å), having a resolution of $\sim 8 \text{ Å}$. The journal of these observations is provided in Table 6. The arc lamp and spectrophotometric standards were also obtained during the observations, and the spectroscopic data reduction was performed using the IRAF software. The pre-processing of raw spectra, extraction of one-dimensional spectra, and the wavelength calibration were done in a standard manner as described in Kumar et al. (2018). For flux

calibration, spectrophotometric standard observations were used. The flux calibrated spectra were then scaled with respect to the calibrated photometric U , B , V , R , and I fluxes to bring them to an absolute flux scale and, finally, corrected for the host galaxy redshift. In this study, we have also used two early epoch archival spectra obtained using the OSIRIS⁵ at GTC-10.4m (Poidevin et al. 2020b) and DBSP⁶ at P200-5.1m (Dahiwalé & Fremling 2020) and downloaded from the Transient Name Server (TNS)⁷.

3 LIGHT CURVE EVOLUTION AND COMPARISON WITH OTHER EVENTS

SN 2020ank was discovered on 2020 January 19 UT 09:15:13 (MJD = 58,867.386) in the observed-frame g -band at $\sim 20.91 \pm 0.30 \text{ mag}$ by the ZTF (Poidevin et al. 2020a). Whereas, the last non-detection was on 2020 January 19 UT 08:09:24 (MJD = 58,867.340) also reported by the ZTF with a r -band upper limit of $\sim 20.40 \text{ mag}$. The host galaxy of SN 2020ank is faint (g -band upper limit $\sim 24 \text{ mag}$) as it was not observed up to the detection limits of Sloan Digital Sky Survey (SDSS), PS1, and Dark Energy Spectroscopic Instrument (DESI) Legacy Survey (Poidevin et al. 2020b). Using this brightness limit, we constrain the explosion date ($\text{MJD}_{\text{expl}} \approx 58857.9$) by extrapolating the pre-maximum rest-frame g -band light curve of SN 2020ank down to the limiting magnitude of the host galaxy by fitting a high-order spline function, as also described in Gezari et al. (2009); Kumar et al. (2020). Our observations of SN 2020ank in the Bessell U , B , V , R , and I bands span $+2.8$ to $+51.6 \text{ d}$ (in the rest-frame). Log of the photometric observations is tabulated in Table 3. For a better sampling, we also used the publicly available photometric SDSS g and r bands data (between

³ DAOPHOT stands for Dominion Astrophysical Observatory Photometry

⁴ <https://lasair.roe.ac.uk/object/ZTF20aahbfmf/>

⁵ Optical System for Imaging and low Resolution Integrated Spectroscopy

⁶ Double Spectrograph

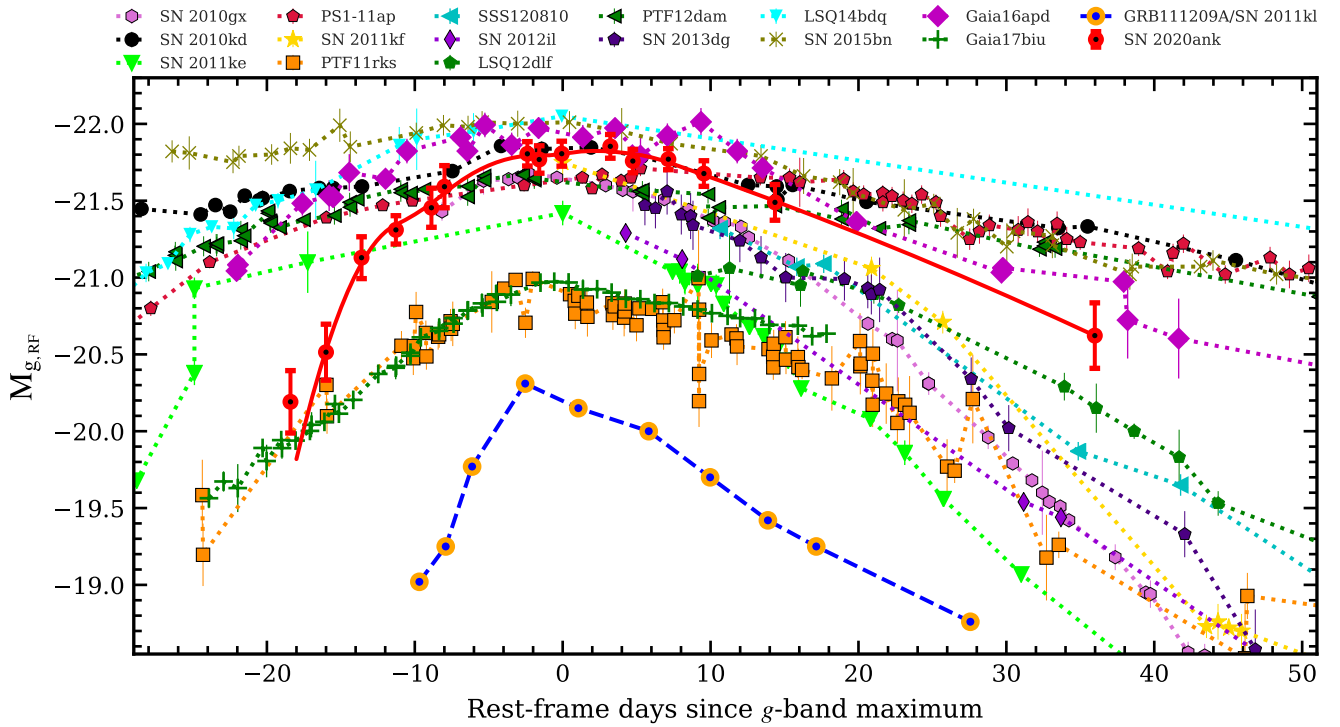
⁷ <https://wis-tns.weizmann.ac.il/>

Table 1. Observing facilities and instruments detail used for the follow-up observations of SN 2020ank.

Facility	Location	Instrument	Gain (e^-/ADU)	Readout Noise (e^-)	Plate scale (arcsec pixel $^{-1}$)	Field of view (arcmin 2)
1.04-m Sampurnanand Telescope	Manora Peak, Nainital	4K×4K Imager	3.0	10.0	0.230	15 × 15
2.0-m Himalayan Chandra Telescope	Hanle, Leh	HFOSC	0.28	5.75	0.296	10 × 10
3.6-m Devasthal Optical Telescope	Devasthal, Nainital	4K×4K Imager	5.0	10.0	0.195	6.5 × 6.5

Table 2. Identification number (ID) and calibrated magnitudes of the secondary standard stars in the field of SN 2020ank as displayed in the left panel of Figure 1.

Star ID	U (mag)	B (mag)	V (mag)	R (mag)	I (mag)
1	17.749 ± 0.010	17.353 ± 0.005	16.615 ± 0.003	16.152 ± 0.005	15.770 ± 0.008
2	17.853 ± 0.017	17.450 ± 0.005	16.662 ± 0.006	16.229 ± 0.007	15.854 ± 0.008
3	17.747 ± 0.010	17.765 ± 0.007	17.208 ± 0.009	16.879 ± 0.008	16.579 ± 0.009
4	18.226 ± 0.010	17.798 ± 0.004	16.953 ± 0.007	16.471 ± 0.006	16.008 ± 0.007
5	17.123 ± 0.009	17.069 ± 0.005	16.512 ± 0.006	16.205 ± 0.004	15.909 ± 0.006
6	—	18.918 ± 0.006	18.405 ± 0.005	18.095 ± 0.010	17.796 ± 0.009
7	—	18.985 ± 0.011	18.302 ± 0.004	17.922 ± 0.007	17.569 ± 0.011

**Figure 2.** Comparison of the rest-frame M_g light-curve of SN 2020ank with other well studied SLSNe I (taken from Nicholl et al. 2015a, 2016; De Cia et al. 2018; Kangas et al. 2017; Bose et al. 2018; Kumar et al. 2020 and references therein) and the long GRB connected SLSN 2011kl (Greiner et al. 2015; Kann et al. 2019). All the presented light-curves are corrected for the Galactic extinction, and the K -corrections also have been applied. SN 2020ank appears to have comparatively brighter $M_{g,peak}$ and faster pre-peak rising and post-peak decaying rates, apparently similar to SN 2010gx and other fast-evolving SLSNe I.

~ -21 to +36 d, from rest-frame) observed by the ZTF (Poidevin et al. 2020a).

The occurrence of SN 2020ank at $z = 0.2485$ (Dahiwalé & Fremling 2020) necessitated the use of applying K -corrections to obtain the rest-frame magnitudes. We estimated K -corrections using the optical spectra of SN 2020ank with help of the light version of SuperNova Algorithm for K -correction Evaluation code (SNAKELOOP; Inserra et al. 2018a) based on the equation given by Hogg et al. (2002). The spectra had been flux calibrated by scaling

them to the photometric data before being used as an input to the SNAKELOOP code. The estimated K -correction terms using the near peak-spectrum (at -0.74 d, in the rest-frame) of SN 2020ank for U , B , g , V , r , R , and I bands are tabulated in Table 4. The K -correction terms for intervening photometric epochs are obtained using the interpolation technique. However, for the photometric data points outside the spectral range we used the same K -correction term obtained for the last available spectral epoch. Using the K -correction magnitude values, we converted $U \rightarrow UVW1_{RF}$, $B \rightarrow U_{RF}$, $g \rightarrow$

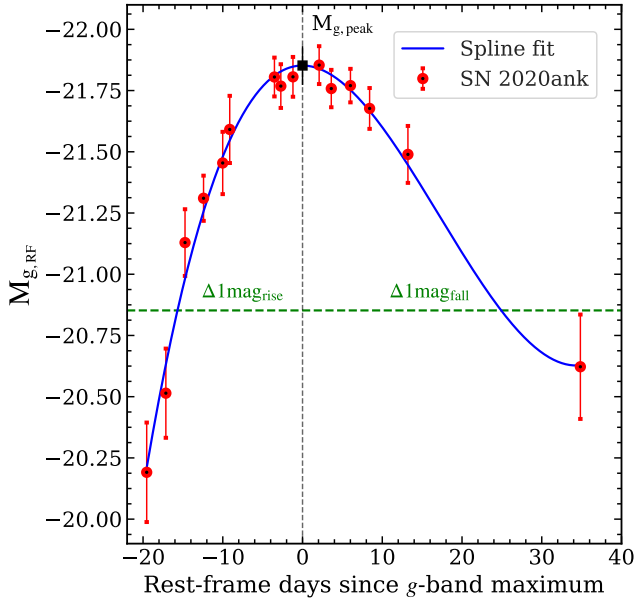


Figure 3. The rest-frame M_g light-curve of SN 2020ank fitted with the third order spline function to calculate the $M_{g,peak}$, $t_{rise}^{\Delta mag}$ and $t_{fall}^{\Delta mag}$ is shown. The black square shows the estimated $M_{g,peak}$, whereas the intersect points of green dotted line and spline fit (in blue) present magnitude values constraining $t_{rise}^{\Delta mag}$ and $t_{fall}^{\Delta mag}$ (in rest-frame d).

u_{RF} , $V \rightarrow B_{RF}$, $r \rightarrow g_{RF}$, $R \rightarrow V_{RF}$ and $I \rightarrow R_{RF}$ bands by applying the formula,

$$M_{RF} = m_O - (5 \times \log d_L + 25) - A_O - K_{OR}, \quad (1)$$

where M_{RF} represents the absolute magnitude in the rest-frame band, m_O is the apparent magnitude in the observed-frame band, d_L is the luminosity distance, A_O is the extinction from the observed band, and K_{OR} is the K -correction term estimated from the spectra of SN 2020ank using the SNAKELOOP code. The data have been corrected for the Galactic extinction using $E(B - V) = 0.023$ mag (Schlafly & Finkbeiner 2011). The weak host emission lines (Osterbrock 1989) and insignificant Na I absorption (Poznan-ski et al. 2012) in near peak spectra of SN 2020ank implied negligible host extinction.

For SN 2020ank, the multiband ($UVW1_{RF}$, u_{RF} , U_{RF} , B_{RF} , g_{RF} , V and R_{RF}) rest-frame absolute magnitudes (after extinction and K -correction) estimated using equation 1 are plotted in the right panel of Figure 1. The phases after correcting for time dilation is plotted with respect to the g -band maximum. From here onward, the discussed bands and the phase will be referred to the rest-frame. A low-order polynomial was fitted around the approximate rest-frame g -band peak brightness to estimate the date of g -band maximum. The date of maximum and the peak magnitude are estimated as $MJD_{g,peak} \approx 58,894.28 \pm 0.15$ and $M_{g,peak} \approx -21.84 \pm 0.10$ mag, respectively. In the u -band, SN 2020ank reached a peak brightness of $M_{u,peak} \approx -21.95 \pm 0.07$ mag on $MJD_{u,peak} \approx 58,893.36 \pm 0.20$. The UV bands appear to peak earlier compared to the redder bands, as found in other CCSNe (Taddia et al. 2018). For SN 2020ank, the $M_{g,peak}$ is consistent with the range of peak absolute magnitudes typically found in the case of other well-studied SLSNe I (Quimby et al. 2013; Nicholl et al. 2016; Inserra et al. 2018b). We observed the post-peak light-curve evolution of SN 2020ank in $UVW1$, U ,

Table 3. Optical-photometric data of SN 2020ank in Bessell U , B , V , R and I bands observed using the ST-1.04, HCT-2.0 and DOT-3.6m. The values presented here are not corrected for Galactic extinction and K -corrections. It is also to be noted that the source could not be observed beyond 2020 April 19 due to the unforeseen situation of COVID-19.

JD	Date	mag	error	Filter	Telescope
2458900.117	2020 February 20	17.879	0.041	U	HCT-2.0m
2458901.133	2020 February 21	17.886	0.072	U	HCT-2.0m
2458912.094	2020 March 16	20.501	0.062	U	DOT-3.6m
2458928.209	2020 March 19	20.856	0.071	U	DOT-3.6m
2458901.133	2020 February 21	18.455	0.035	B	HCT-2.0m
2458911.343	2020 March 02	18.930	0.028	B	HCT-2.0m
2458912.094	2020 March 03	18.998	0.021	B	HCT-2.0m
2458912.193	2020 March 03	19.069	0.030	B	DOT-3.6m
2458925.109	2020 March 16	20.134	0.021	B	DOT-3.6m
2458928.209	2020 March 19	20.402	0.023	B	DOT-3.6m
2458956.212	2020 April 16	22.797	0.093	B	DOT-3.6m
2458898.229	2020 February 18	18.542	0.149	V	ST-1.04m
2458900.117	2020 February 20	18.466	0.021	V	HCT-2.0m
2458901.133	2020 February 21	18.526	0.020	V	HCT-2.0m
2458911.343	2020 March 02	18.690	0.023	V	HCT-2.0m
2458912.094	2020 March 03	18.753	0.021	V	HCT-2.0m
2458912.094	2020 March 16	18.758	0.019	V	DOT-3.6m
2458928.209	2020 March 19	19.502	0.020	V	DOT-3.6m
2458956.212	2020 April 16	21.489	0.035	V	DOT-3.6m
2458898.229	2020 February 18	18.307	0.070	R	ST-1.04m
2458900.117	2020 February 20	18.389	0.019	R	HCT-2.0m
2458901.133	2020 February 21	18.373	0.029	R	HCT-2.0m
2458911.343	2020 March 02	18.611	0.026	R	HCT-2.0m
2458912.094	2020 March 03	18.642	0.029	R	HCT-2.0m
2458912.193	2020 March 03	18.593	0.021	R	DOT-3.6m
2458925.109	2020 March 16	18.994	0.019	R	DOT-3.6m
2458928.209	2020 March 19	19.109	0.020	R	DOT-3.6m
2458955.197	2020 April 15	20.673	0.026	R	DOT-3.6m
2458956.212	2020 April 16	20.665	0.025	R	DOT-3.6m
2458959.178	2020 April 19	20.948	0.027	R	DOT-3.6m
2458898.229	2020 February 18	18.327	0.071	I	ST-1.04m
2458900.117	2020 February 20	18.415	0.025	I	HCT-2.0m
2458901.133	2020 February 21	18.433	0.035	I	HCT-2.0m
2458911.343	2020 March 02	18.574	0.023	I	HCT-2.0m
2458912.094	2020 March 03	18.636	0.027	I	HCT-2.0m
2458912.193	2020 March 03	18.568	0.022	I	DOT-3.6m
2458925.109	2020 March 16	18.847	0.021	I	DOT-3.6m
2458928.209	2020 March 19	18.929	0.023	I	DOT-3.6m
2458955.197	2020 April 15	19.760	0.026	I	DOT-3.6m
2458956.212	2020 April 16	20.670	0.067	I	DOT-3.6m
2458959.178	2020 April 19	20.297	0.059	I	DOT-3.6m

B , V , and R bands and calculated the decay rates. The redder bands seem to have shallower post-peak decay rates in comparison to the UV bands, which is ~ 0.05 and ~ 0.15 mag d^{-1} for the R and $UVW1$ bands, respectively. In the case of SN 2020ank, the redder bands (V and R ; 0.06 and 0.05 mag d^{-1} , respectively) exhibit a steeper post-peak decay rate in comparison to the average g -band post-peak decay rate (for < 60 d, 0.04 mag d^{-1}) for the SLSNe I discussed by De Cia et al. (2018), indicating the comparatively fast-decaying behavior of SN 2020ank. Additionally, the U -band post-peak decay rate of SN 2020ank is well in agreement with the $^{56}Ni \rightarrow ^{56}Co$ theoretical decay curve (0.11 mag d^{-1}), see right panel of Figure 1.

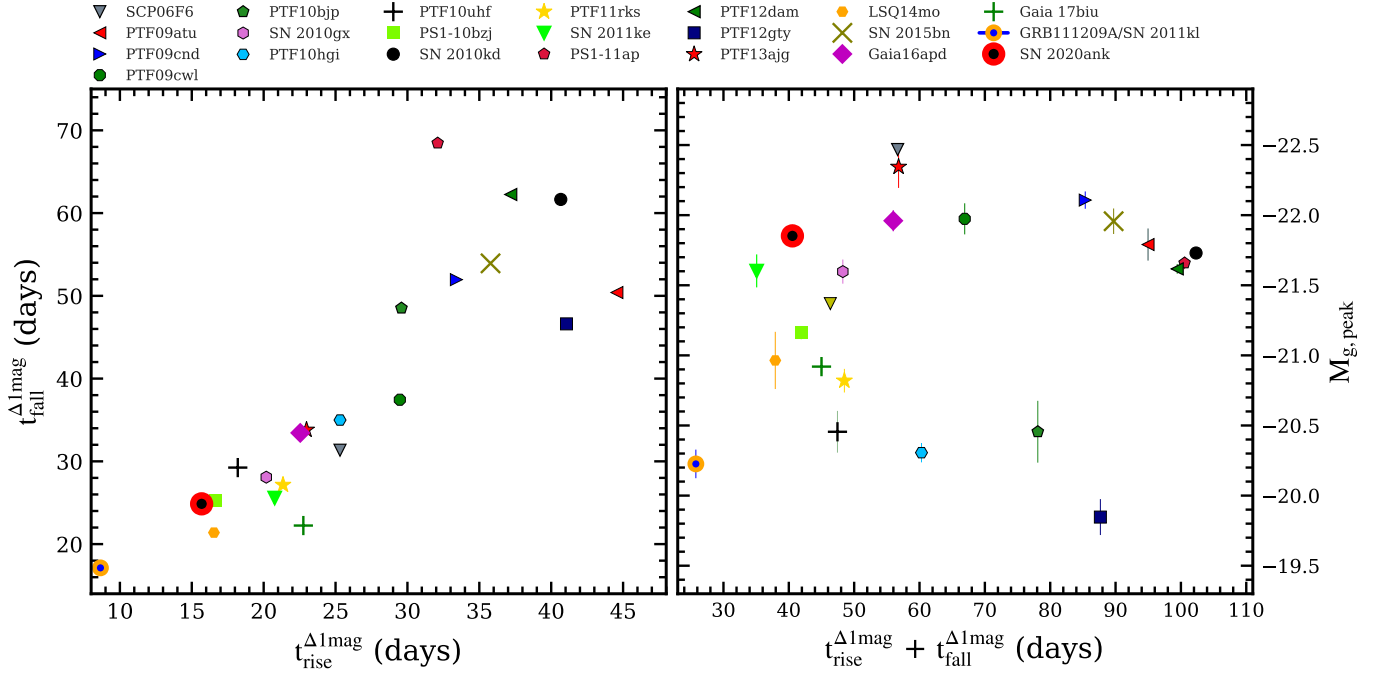


Figure 4. *Left:* Estimated values of $t_{\text{fall}}^{\Delta\text{mag}}$ compared with $t_{\text{rise}}^{\Delta\text{mag}}$ indicating nearly a linear relation between the two observed quantities for the set of SLSNe I. *Right:* The sum of $t_{\text{fall}}^{\Delta\text{mag}}$ and $t_{\text{rise}}^{\Delta\text{mag}}$ compared with $M_{g,\text{peak}}$ does not show any such correlation. However, from these plots, it is clear that SN 2020ank is a fast-evolving SLSN with a comparatively brighter peak. On the other hand, the GRB connected SLSN 2011kl (Greiner et al. 2015; Kann et al. 2019) seems to have the fastest pre-peak rising and post-peak decaying rates in comparison to all other presented SLSNe I.

Table 4. Estimated values of K -corrections (in magnitudes) for different passbands are listed. The values were determined using the near-peak spectrum (at -0.74 d) of SN 2020ank using the SNAKELOOP code (Inserra et al. 2018a).

Observed band	Rest-frame band	K -correction (mag)
U (Vega)	$UVW1$ (Vega)	0.57 ± 0.02
B (Vega)	U (Vega)	0.75 ± 0.01
g (AB)	u (AB)	-0.17 ± 0.01
V (Vega)	B (Vega)	-0.28 ± 0.01
r (AB)	g (AB)	-0.22 ± 0.01
R (Vega)	V (Vega)	-0.44 ± 0.01
I (Vega)	R (Vega)	-0.49 ± 0.03

3.1 The rest-frame M_g light-curves

We compare the rest-frame g -band absolute magnitudes of SN 2020ank with well-studied bright ($M_{g,\text{peak}} > -20.5$ mag) SLSNe I taken from Nicholl et al. 2015a, 2016; De Cia et al. 2018; Kangas et al. 2017; Bose et al. 2018; Kumar et al. 2020 and references therein (see Figure 2). We also compare the M_g light-curve of SN 2020ank with the only known SLSN 2011kl associated with a long-duration GRB 111209A (Greiner et al. 2015; Kann et al. 2019). For SLSNe I having Bessell B -band data, the transformation equations and uncertainties by Jordi et al. (2006) have been used to obtain the SDSS g -band magnitudes. Figure 2 shows that SN 2020ank is a bright SLSN with $M_{g,\text{peak}} \sim -21.84 \pm 0.10$ mag, which is closer to SN 2010kd (Kumar et al. 2020) and Gaia16apd (Kangas et al. 2017; Nicholl et al. 2017a) within errors, whereas, fainter than LSQ14bdq (Nicholl et al. 2015b) and

SN 2015bn (Nicholl et al. 2016). SN 2020ank appears to have steeper pre-peak rising and post-peak decaying rates similar to that observed for other fast-evolving SLSNe I (e.g., SN 2011ke). Further, the post-peak decay rate of SN 2020ank is also steeper in comparison to slow-evolving SLSNe I such as SN 2010kd (Kumar et al. 2020), PTF12dam (Nicholl et al. 2013), and SN 2015bn (Nicholl et al. 2016).

To constrain the peak brightness, rise and decay times of a larger sample of such SLSNe I (present case and those discussed in Nicholl et al. 2015a; De Cia et al. 2018), we independently estimate the $M_{g,\text{peak}}$ and time taken to rise/decay by 1 mag to/from the peak absolute magnitudes ($t_{\text{rise}}^{\Delta\text{mag}}/t_{\text{fall}}^{\Delta\text{mag}}$) using the rest-frame M_g light curves. To estimate the values of $M_{g,\text{peak}}$, $t_{\text{rise}}^{\Delta\text{mag}}$ and $t_{\text{fall}}^{\Delta\text{mag}}$, we fitted a low-order spline function to the rest-frame M_g light curves (see Figure 3, also discussed by De Cia et al. 2018). SLSNe I having less pre- or post-peak data are omitted, but a sparse extrapolation was done wherever necessary. We plot the $t_{\text{fall}}^{\Delta\text{mag}}$ with respect to $t_{\text{rise}}^{\Delta\text{mag}}$ and their sum with $M_{g,\text{peak}}$ in the left and right panels of Figure 4, respectively. Generally, SLSNe I with higher values of $t_{\text{rise}}^{\Delta\text{mag}}$ also display the higher values of $t_{\text{fall}}^{\Delta\text{mag}}$ as also discussed by Nicholl et al. 2015a; De Cia et al. 2018, whereas no such correlation appears between $t_{\text{rise}}^{\Delta\text{mag}} + t_{\text{fall}}^{\Delta\text{mag}}$ and $M_{g,\text{peak}}$.

SN 2020ank exhibits the steepest pre-peak rising rate (lower value of $t_{\text{rise}}^{\Delta\text{mag}}$) in comparison to other SLSNe-I in the sample, except for the GRB-associated SLSN 2011kl (Kann et al. 2019). The right panel of Figure 4 also shows that SN 2020ank exhibits a faster photometric evolution (lower value of $t_{\text{rise}}^{\Delta\text{mag}} + t_{\text{fall}}^{\Delta\text{mag}}$) closer to those seen for PS1-10bzj, LSQ14mo, etc., but has the brightest peak in comparison to all other plotted fast-evolving SLSNe I. In all, SN 2020ank is a fast-evolving SLSN with high peak brightness in the g -band.

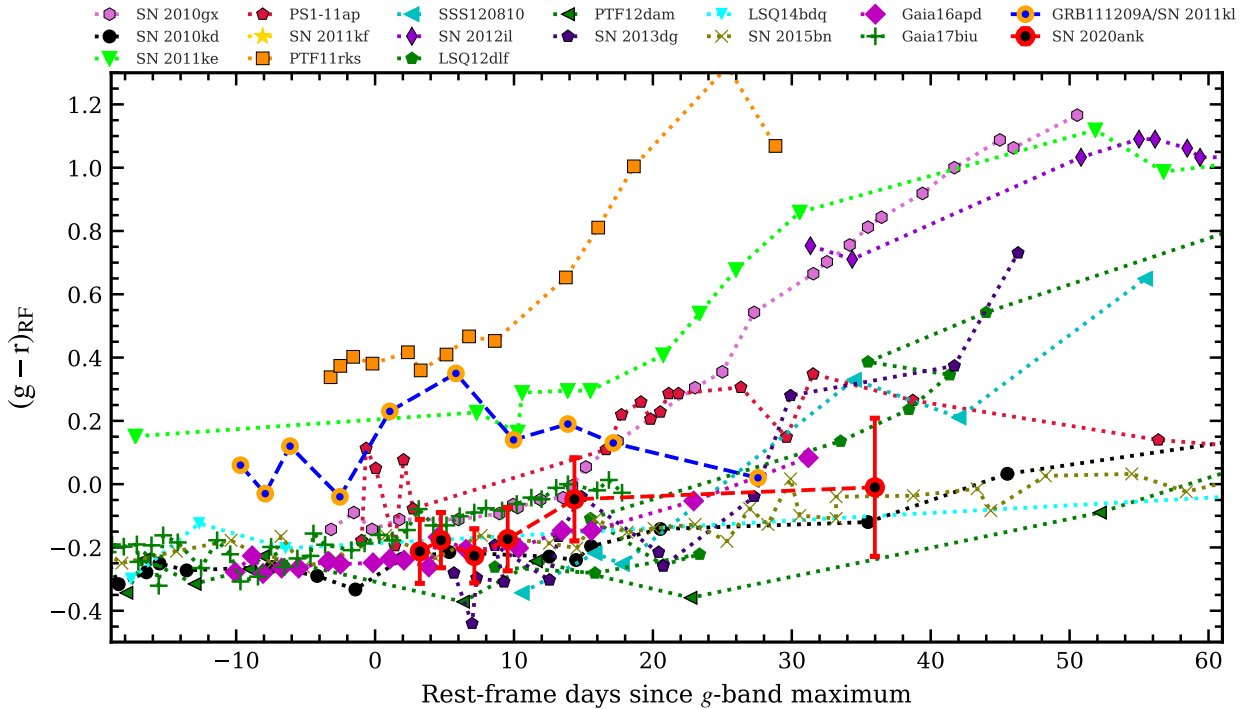


Figure 5. The rest-frame $g-r$ colour evolution of SN 2020ank (in red) along with some other well studied SLSNe I (taken from Nicholl et al. 2015a, 2016; De Cia et al. 2018; Kangas et al. 2017; Kann et al. 2019; Bose et al. 2018; Kumar et al. 2020) is presented (Galactic extinctions and K -corrected). The colour evolution of SN 2020ank seems similar to those found for the slow-evolving SLSNe I.

3.2 The rest-frame $g-r$ colour evolution

During the photospheric phase, optical-NIR colours are useful probes to understand the temperature evolution of SLSNe. Due to the unavailability of the rest-frame r -band data for SN 2020ank, the rest-frame (Galactic extinction and K -corrected) V and R bands data were transformed to the r -band magnitudes using the transformation equation and uncertainties given by Jordi et al. (2006). So, here we compare the rest-frame $g-r$ colour evolution of SN 2020ank with that observed for the well studied SLSNe I (see Figure 5). The slow-evolving SLSNe I (SN 2010kd, PTF12dam, SN 2015bn, etc.) appear to have shallower rising (from blue to red) colour evolution (from ~ -0.4 to 0.2 mag in a time range of ~ -20 to $+100$ d). In contrast, the fast-evolving SLSNe I (e.g., SN 2010gx, SN 2011ke, 2012il, etc.) show $g-r$ colour ranging from ~ 0.0 to $\gtrsim 1.2$ mag in the same temporal bin. SN 2020ank presents a bluer $g-r$ colour evolution from $\sim +3$ to $+36$ d spanning the range -0.3 to 0.1 mag. Overall, the $g-r$ colour of the fast-evolving SN 2020ank is closer to the slow-evolving SLSNe I. The rest-frame $UVW1-r$ colour evolution of SN 2020ank is also discussed in section 3.3.

3.3 Comparison of UV-brightness

In this section, we compare the rest-frame equivalent $UVW1$ brightness and evolution of the $UVW1-r$ colour of SN 2020ank with other well-studied SLSNe I (see Figure 6). Near the peak, $UVW1$ brightness of SN 2020ank appears to be comparable to Gaia16apd, the most UV bright SLSN to date (Nicholl et al. 2017a) except the most luminous SLSN ASASSN-15lh (Dong et al. 2016). With time, the $UVW1$ flux of SN 2020ank decays very sharply and becomes fainter in comparison to other presented SLSNe I (except PTF12dam and SN 2011kl), see the upper panel of Figure 6. One of

the possible reasons behind this excess UV flux of SN 2020ank near the peak may be the lower production of heavier group elements during the explosion, as suggested by Yan et al. (2017a) in the case of Gaia16apd (see also Mazzali et al. 2016). The other possible reason could be a short-lived powering source adding extra luminosity component towards the UV or lower natal metallicity. However, these plausible reasons for explaining the excess UV flux were not found suitable in the case of Gaia16apd (Nicholl et al. 2017a). This is because of its similar metallicity and degree of spectral absorption features to the other SLSNe I having a lower UV flux. In the case of Gaia16apd, the most likely possible reason might be a central engine as a power source (it could be a spin-down millisecond magnetar with lower spin period and comparatively low mass or a mass accreting BH; MacFadyen & Woosley 1999), which could explain both the overall luminosity and the excess UV flux (Nicholl et al. 2017a). For SN 2020ank as well, the central engine based powering source as a possible mechanism for the observed UV excess near the peak is well in agreement with semi-analytical light-curve modelling results discussed later in section 4.1.

In the lower panel of Figure 6, we compare the $UVW1-r$ colour evolution of SN 2020ank with the well studied SLSNe I. The rest-frame $UVW1-r$ colour curves of PTF12dam, SN 2015bn, and Gaia16apd are taken from Nicholl et al. (2017a), whereas calculated independently for SN 2010kd and Gaia17biu. Due to the unavailability of SDSS r -band data for SN 2020ank and SN 2010kd, we obtained the r -band data from the available V and R bands data using the transformation equations and uncertainties given by Jordi et al. (2006). Before estimating colours, the $UVW1$ magnitudes were converted from Vega to AB system using the zero points adopted from Breeveld et al. (2011). Near the peak, $UVW1-r$ colour of SN 2020ank is closer to those observed in the case of

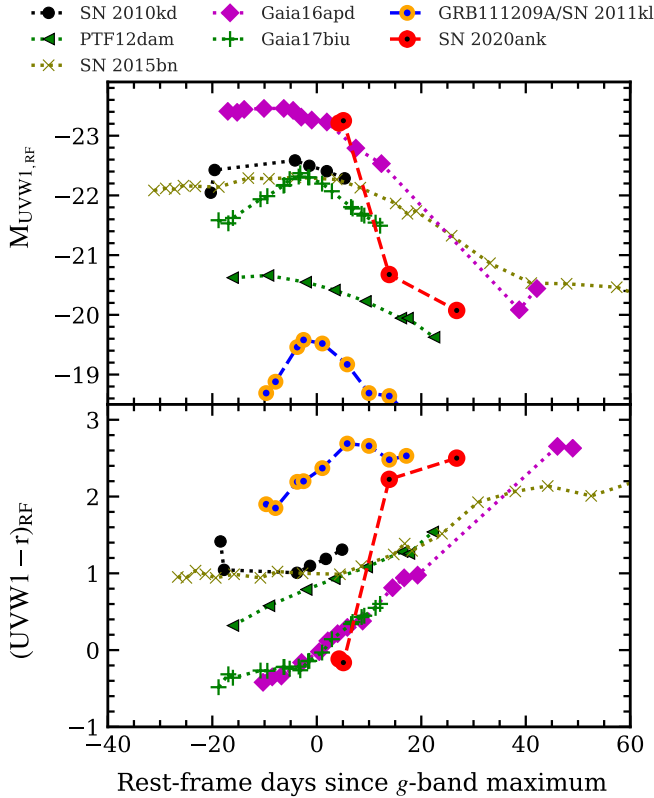


Figure 6. *Upper:* The rest-frame M_{UVW1} light-curve of SN 2020ank (after applying Galactic extinctions and K -corrections) is presented and compared with the following well studied SLSNe I: SN 2010kd (Kumar et al. 2020), SN 2011kl (Greiner et al. 2015; Kann et al. 2019), PTF12dam (Nicholl et al. 2013), SN 2015bn (Nicholl et al. 2016), Gaia16apd (Kangas et al. 2017; Nicholl et al. 2017a) and Gaia17biu (Bose et al. 2018). Near the peak, $UVW1$ brightness of SN 2020ank seems even higher to that observed in the case of Gaia16apd. *Lower:* The rest-frame $UVW1 - r$ colour evolution of SN 2020ank is compared with the same sample of SLSNe I discussed above in the AB magnitude system. Near the peak, SN 2020ank exhibits bluer colour in comparison to other SLSNe I and turns redder very sharply with time.

Gaia16apd and Gaia17biu; however, it is $\sim 1\text{--}2.5$ mag bluer in comparison to other presented SLSNe I. With time, $UVW1 - r$ colours of SN 2020ank turn redder quite sharply, indicating a rapid drop in temperature, also in agreement with the estimate of temperature using the BB fitting to the photometric spectral energy distribution (SED), see section 4 and Figure 8.

4 BOLOMETRIC LIGHT-CURVE

We generate the rest-frame quasi-bolometric ($UVW1, u, U, B, g, V$, and R bands) light-curve of SN 2020ank using a Python-based code Superbol (Nicholl 2018). To compute the multiband fluxes, interpolation or extrapolation was done wherever necessary assuming constant colours to get the magnitudes at the individual epochs using standard methods. The uncertainties in the calculation of zero points are also taken care of by adding 3% uncertainties to the bolometric luminosity error as is suggested by the software release of

Superbol⁸. The pseudo-bolometric ($UVW1$ to R) light-curve of SN 2020ank presents a peak luminosity (L_{max}) of $\sim (1.89 \pm 0.14) \times 10^{44}$ erg s⁻¹. To include the expected flux contribution from UV and NIR regions, we extrapolated the SED (here the BB model) by integrating over the observed fluxes and obtained the full bolometric light curve. The full bolometric light-curve (UV to NIR) of SN 2020ank (in red) between ~ -20 to $+50$ d, derived so, exhibited L_{max} of $\sim (3.89 \pm 0.69) \times 10^{44}$ erg s⁻¹ at MJD ≈ 58892.8 , overall consistent with other well studied SLSNe I, see Figure 7. In the case of SN 2020ank, the bolometric light-curve is nearly symmetric around the peak with the $L_{max}^{rise}/e \approx L_{max}^{fall}/e \approx 15$ d (time taken to rise/decay by L_{max}/e to/from the L_{max}).

For an extensive comparison of bolometric luminosities, the sample used in Figure 2 was supplemented with data of PTF13ajg (Vreeswijk et al. 2014) and ASASSN-15lh (Dong et al. 2016) along with the independently generated bolometric light curves of PTF11rks, SN 2011kf and SN 2012il (Inserra et al. 2013). The comparison shows that SN 2020ank is one of the brightest SLSN with a peak bolometric luminosity higher in comparison to SN 2010kd, PTF12dam, SN 2015bn, etc., but fainter than SN 2011kf, PTF13ajg, and the most luminous SLSN ASASSN-15lh (Dong et al. 2016) in the sample. As obtained from the rest-frame M_g light-curves comparison, SN 2020ank appears to have high pre-peak rising and post-peak decay rates of its bolometric light curve, similar to that of fast-evolving SLSNe I (e.g., SN 2010gx and SN 2011ke). In all, SN 2020ank is a bright SLSN having a bell-shaped light-curve around the peak with a fast-evolving behaviour.

Figure 8 shows the evolution of BB temperature (T_{BB}) and radius (R_{BB}) of SN 2020ank. The T_{BB} and R_{BB} values are calculated by modelling the photometric SED at individual epochs by fitting a BB function using the Superbol code (Nicholl 2018). From ~ -20 d to peak, the T_{BB} of SN 2020ank seems to be constant around $\sim 16,000$ K, whereas, from peak to $\sim +15$ d it sharply decays with a rate of ~ 600 K per d. At later epochs (after $\sim +15$ d), the T_{BB} appears to be constant again at ~ 7000 K. The near peak T_{BB} of SN 2020ank is higher in comparison to well-studied slow-evolving SLSNe I PTF12dam and SN 2015bn (Chen et al. 2015; Nicholl et al. 2016), nearly consistent with intermediate decaying Gaia16apd (Kangas et al. 2017; Nicholl et al. 2017a), and lower than the most luminous SLSN ASASSN-15lh (Dong et al. 2016). On the other hand, from ~ -20 to $+15$ d the value of R_{BB} for SN 2020ank increases from $\sim 1.3 \times 10^{15}$ to 8.8×10^{15} cm, thereafter, up to $\sim +50$ d, it decreases to $\sim 3.4 \times 10^{15}$ cm.

4.1 Light-curve modelling using MINIM

We attempt to reproduce the bolometric light curve of SN 2020ank with the RD, MAG, constant density CSMI (CSMI0), and wind-like CSMI (CSMI2) semi-analytical light curve models (see Figure 9) using the MINIM code (Chatzopoulos et al. 2013). MINIM is a general-purpose fitting code that finds the global solution for non-linear χ^2 fitting. It uses the Price algorithm (Brachetti et al. 1997), a controlled random-search technique, to look for the global minimum of the χ^2 hyper-surface within the allowed parameter volume. After that, parameters generated by the Price algorithm for the lowest χ^2 value are fine-tuned by the Levenberg-Marquardt algorithm (Moré 1978), which gives the final set of parameters for the best-fitted model. The uncertainties in the parameters are estimated us-

⁸ <https://github.com/mnicholl/superbol>

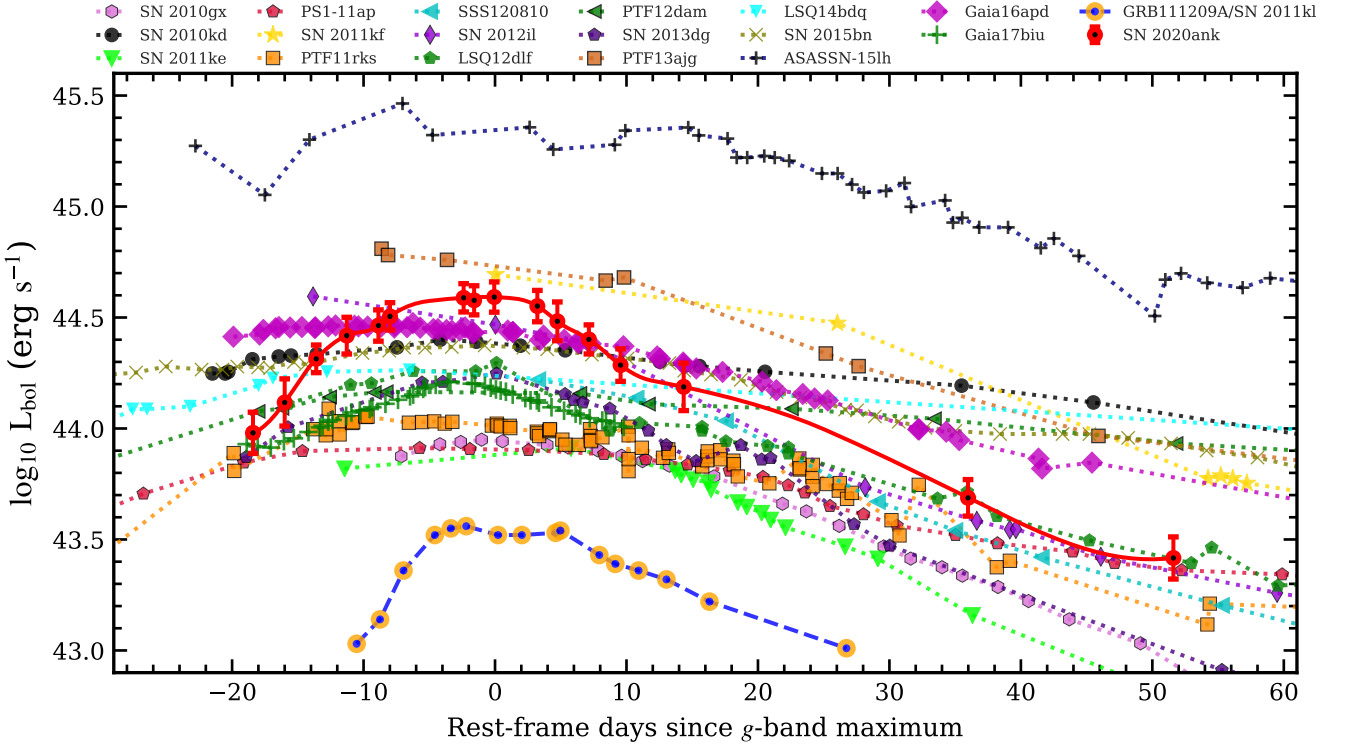


Figure 7. The rest-frame bolometric light-curve of SN 2020ank (*UV* to *NIR*) and its comparison with a sample of other well-studied SLSNe I taken from Vreeswijk et al. 2014; Nicholl et al. 2015a; Dong et al. 2016; Nicholl et al. 2016; De Cia et al. 2018; Kangas et al. 2017; Bose et al. 2018; Kann et al. 2019; Kumar et al. 2020 are presented. The comparison indicates that SN 2020ank is one of the brightest SLSN though fainter than SN 2011kf (Inserra et al. 2013), PTF13ajg (Vreeswijk et al. 2014) and ASASSN-15lh (Dong et al. 2016).

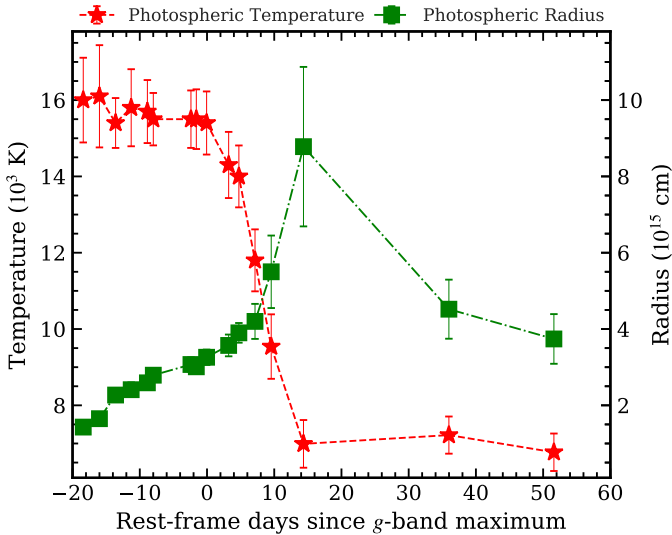


Figure 8. The photospheric temperature (T_{BB}) and radius (R_{BB}) evolution of SN 2020ank are presented, through BB fit to the photometric data using the Superbol code (Nicholl 2018).

ing the standard deviation of the random vectors around the global minimum. Details about the above discussed models, MINIM code and fitting procedures are described in Chatzopoulos et al. (2012, 2013).

For all the models discussed above, we adopted the electron-scattering opacity, $\kappa = 0.1 \text{ cm}^2 \text{ g}^{-1}$, by considering half ionized

elements for SLSNe I (Inserra et al. 2013; Nagy 2018). For RD and MAG models, the M_{ej} values are estimated using equation 10 of Chatzopoulos et al. (2012), where the integration constant (β) was considered to be 13.8. In the case of RD model, v_{exp} is taken equals to $12,000 \text{ km s}^{-1}$ as obtained from the spectral analysis of SN 2020ank discussed in section 5.1. However, for the MAG model, v_{exp} was given by the MINIM itself as a fitting parameter. The initial period of the new-born magnetar in ms (P_i) is given by $P_i = 10 \times (\frac{2 \times 10^{50} \text{ erg s}^{-1}}{E_p})^{0.5}$, where E_p is the magnetar rotational energy in erg. The magnetic field of the millisecond magnetar in Gauss units (B) is estimated by $B = 10^{14} \times (\frac{130 \times P_i^2}{t_{p,yr}})^{0.5}$, where $t_{p,yr}$ is the magnetar spin-down timescale in years.

It is evident from Figure 9 that all four models (RD, MAG, CSM10, and CSM12) fit the data adequately, i.e., with $\chi^2/\text{DOF} \sim 1$. Here, we caution that in the present case, the χ^2/DOF is used as an indicator for selecting the model parameters that fit the data best and not as a statistical probe for judging the significance of the models. In this situation, the best χ^2 value solely cannot be used as a criterion to declare the most probable model. Therefore, we look for the feasibility of various physical parameters retrieved from different models. The parameters obtained from the MINIM modelling using the four discussed models are tabulated in Table 5. In the RD model, the calculated M_{ej} is lower than M_{Ni} (see Table 5), an un-physical case, so we exclude RD's possibility as a possible powering mechanism for SN 2020ank. The CSM10 and CSM12 models also well reproduced the bolometric light-curve of SN 2020ank though some of the derived parameters seem quite unphysical (e.g., very high values of R_p , M_{ej} , v_{exp} and \dot{M}). For both the models, M_{ej} and v_{exp} values are very high, that correspond to

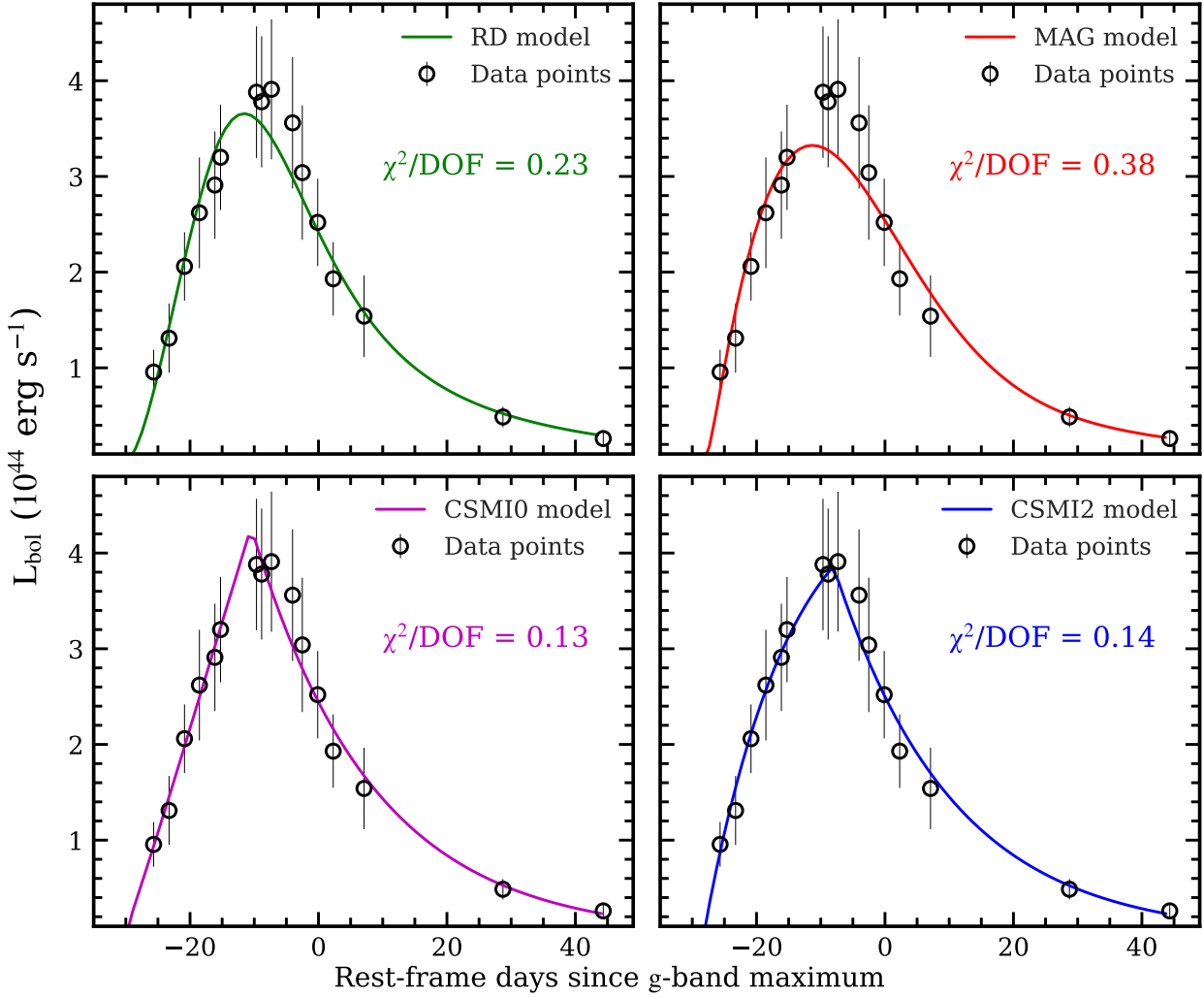


Figure 9. Semi-analytic light curve models (RD, MAG, CSM10 and CSM12) are fitted to the bolometric light curve of SN 2020ank using the MINIM code (Chatzopoulos et al. 2013). For all the model fittings, the $\kappa = 0.1 \text{ cm}^2 \text{ g}^{-1}$ is adopted. All four discussed models well reproduced the bolometric light-curve of SN 2020ank with $\chi^2/\text{DOF} \sim 1$; but, the physical reliability of the derived parameters suggested the MAG model as the most suitable one for SN 2020ank.

the kinetic energy of a few $\times 10^{53}$ erg, an inadmissible amount for CCSNe (Janka 2012). Besides this, values of M_{ej} and v_{exp} obtained from CSM10 and CSM12 model fits are also higher than those from our spectral analysis in section 5. The estimated values of R_p are also in the order of $\sim 10^{15}$ cm ($\gtrsim 35,000 R_{\odot}$; see Table 5), which is very high and close to the radius of the H-rich CSM shells, making it un-physical in the present case (Yan et al. 2017b; Nicholl et al. 2019). The CSM10 model gives rise to an unacceptable amount of $\dot{M} \sim 55 M_{\odot} \text{ yr}^{-1}$. Though, the CSM12 model has a comparatively lower \dot{M} ($\sim 0.6 M_{\odot} \text{ yr}^{-1}$), but this is also an unreasonably higher rate before the explosion. All these factors indicate that CSM10 and CSM12 models are not favored to explain the light-curve of SN 2020ank. On the other hand, around the peak the MAG model poorly fits the bolometric light-curve of SN 2020ank because of its bell-shaped ($L_{\text{max}}^{\text{rise}} \approx L_{\text{max}}^{\text{fall}} \approx 15$ d) layout (Chatzopoulos & Tuminello 2019). But, the MAG model presents a reasonable set of physical parameters among all these discussed four MINIM models. The estimated parameters by the MAG model for SN 2020ank (see Table 5) are within the range of parameters found for other well studied SLSNe I (see section 4.1.1) and close with the cor-

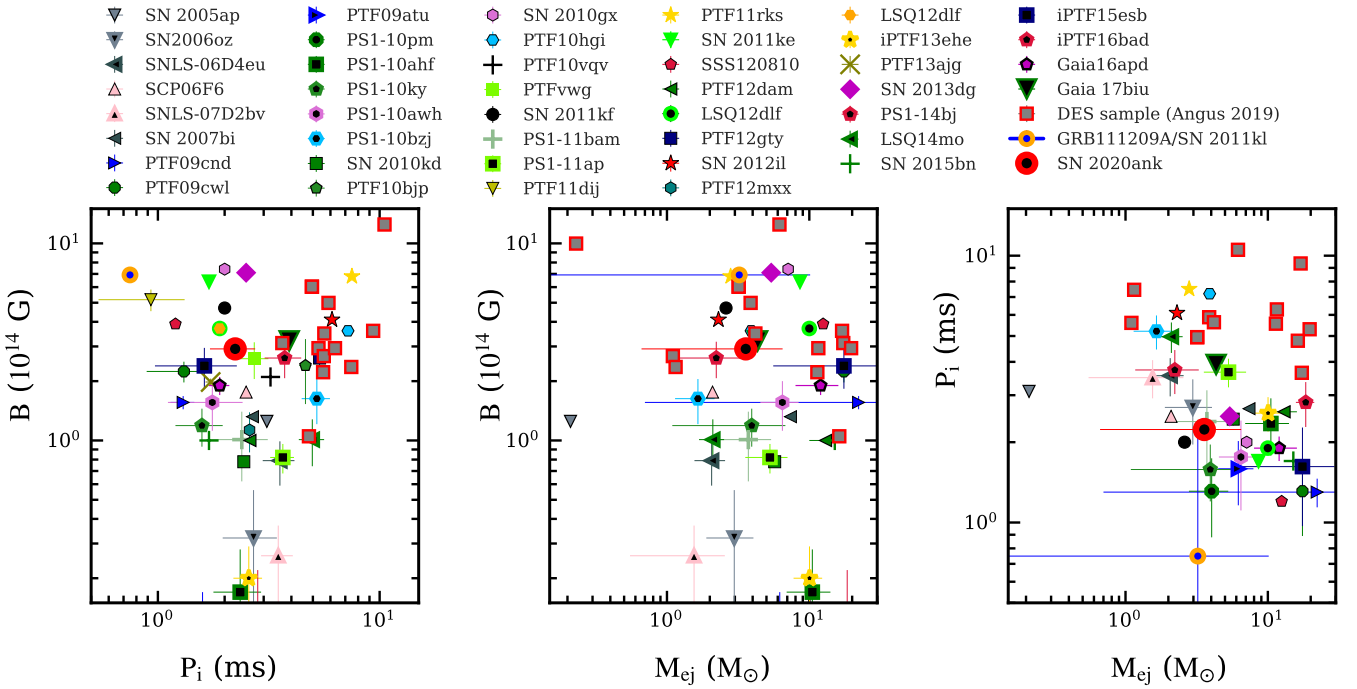
responding parameters obtained from the spectral analysis in section 5. The spin-down millisecond magnetar as a possible powering source for SN 2020ank is also consistent with the excess UV flux of SN 2020ank near the peak favoring a central engine based power source (see section 3.3).

In summary, based on our fitting we consider the MAG model as the most probable one because 1) it fits the data well ($\chi^2/\text{DOF} \sim 1$), and 2) its parameters are realistic and closer to the ones inferred from the spectral modelling (M_{ej} , v_{exp} ; see section 11). So, the spin-down millisecond magnetar is found to be the most suitable powering source for SN 2020ank with P_i of $\sim 2.23 \pm 0.51$ ms and $B \sim (2.91 \pm 0.07) \times 10^{14}$ G, giving rise to an ejected mass of $\sim 3.58 \pm 0.04 M_{\odot}$. The MAG model suggests the value of progenitor radius (R_0) $\sim (2.8 \pm 2.2) \times 10^{12}$ cm, nearly forty times the solar radius, whereas other parameters are tabulated in Table 5 in bold.

Table 5. Best-fit parameters for the RD, MAG, CSM10 and CSM12 models obtained using the MINIM fitting.

A_γ ^a	M_{ej} ^b (M_\odot)	t_d ^c (d)	RD model					χ^2/DOF
			M_{Ni} (M_\odot)					
9.20 ± 1.34	2.62 ± 0.38	21.66 ± 1.55	26.71 ± 2.55					0.23
MAG model								
R_0 (10 ¹³ cm)	M_{ej} (M_\odot)	E_p ^d (10 ⁵¹ erg)	t_d (d)	t_p ^e (d)	v_{exp} (10 ³ km s ⁻¹)	P_i (ms)	B (10 ¹⁴ G)	χ^2/DOF
0.28 ± 0.22	3.58 ± 0.04	4.02 ± 0.19	25.01 ± 0.16	2.79 ± 0.35	12.27 ± 0.91	2.23 ± 0.51	2.91 ± 0.07	0.38
R_p ^f (10 ¹³ cm)	M_{ej} (M_\odot)	M_{csm} ^g (M_\odot)	\dot{M} ^h (M_\odot yr ⁻¹)		v_{exp} (10 ³ km s ⁻¹)			χ^2/DOF
CSMI0 model								
263.20 ± 45.57	46.13 ± 7.78	9.13 ± 1.56	54.95 ± 11.32		29.69 ± 1.84			0.13
CSMI2 model								
312.90 ± 19.87	45.11 ± 8.93	13.12 ± 0.83	0.58 ± 0.05		23.23 ± 0.59			0.14

^a A_γ : optical depth for the gamma-rays measured after the 10 d of explosion. ^b M_{ej} : ejecta mass (in M_\odot). ^c t_d : effective diffusion timescale (in d). ^d E_p : magnetar rotational energy (in 10^{51} erg). ^e t_p : magnetar spin-down timescale (in d). ^f R_p : progenitor radius before the explosion (in 10^{13} cm). ^g M_{csm} : CSM mass (in M_\odot). ^h \dot{M} : progenitor mass-loss rate (in M_\odot yr $^{-1}$).

**Figure 10.** Scatter plot showing the comparison of P_i , B and M_{ej} values derived for SN 2020ank using the semi-analytical light-curve MINIM modelling with the sample of the well studied SLSNe I is presented.

4.1.1 Comparison of derived physical parameters with other SLSNe I

In this section, we compare the P_i , B and M_{ej} of SN 2020ank estimated through semi-analytical light-curve modelling using MINIM with those found in case of other well-studied SLSNe I (see Figure 10): SN 2005ap, SCP06F6, SN 2007bi (Chatzopoulos et al. 2013), SN 2010gx, PTF10hgi, PTF11rks, SN 2011ke, SN 2011kf, SN 2012il (Inserra et al. 2013), PTF12dam (Nicholl et al. 2013), LSQ12dlf, SSS120810, SN 2013dg (Nicholl et al. 2014),

SN 2015bn (Nicholl et al. 2016), Gaia16apd (Kangas et al. 2017), SN 2006oz, SNLS-07D2bv, SNLS-06D4eu, PTF09atu, PS1-10pm, PS1-10ahf, PS1-10ky, PS1-10awh, PS1-10bzj, PS1-11bam, PS1-11ap, LSQ12dlf, iPTF13ehe, PS1-14bj, LSQ14mo, iPTF15esb, iPTF16bad (Nicholl et al. 2017b), Gaia17biu (Wheeler et al. 2017), PTF09cnd, PTF09cwl, PTF10bjp, PTF10vqv, PTF10vvg, PTF11dij, PTF12gty, PTF12mxx, PTF13ajg (De Cia et al. 2018), SN 2010kd (Kumar et al. 2020) and the sample of SLSNe I from the Dark Energy Survey (DES; Angus et al. 2019). We also con-

sider SN 2011kl for comparison, as this is the only case having confirmed association of a SLSN with a long GRB, favouring a central engine driven powering source (Bersten et al. 2016; Lin et al. 2020; Kann et al. 2019). However, we also caution that distinct methods were used in different studies to estimate these parameters.

In the left panel of Figure 10, we present P_i versus B derived for SN 2020ank with other well studied SLSNe I discussed above, whereas, middle and right panels show comparisons of the M_{ej} versus B and P_i , respectively. Most of the SLSNe I presented here have P_i and B values varying in the range of ~ 1 –8 ms and $\sim (1$ –8) $\times 10^{14}$ Gauss, respectively, whereas M_{ej} values vary from ~ 1 to 25 M_\odot . Overall, most of the slow-evolving SLSNe I (e.g., SN 2010kd and SN 2015bn) appear to have larger M_{ej} values in comparison to those exhibited by the fast-evolving SLSNe I (e.g., SN 2010gx and SN 2011kf), as also stated by Könyves-Tóth & Vinkó (2020). In the case of SN 2020ank, the values of P_i ($\sim 2.23 \pm 0.51$ ms), B ($\sim (2.91 \pm 0.07) \times 10^{14}$ G) and M_{ej} ($\sim 3.58 \pm 0.04 M_\odot$) are consistent with those found for other well studied SLSNe I. However, the P_i value of SN 2020ank is closer to PS1-10ahf and PS1-11bam, the B is similar to DES14X3taz and DES17C3gyp (Angus et al. 2019), and the M_{ej} is consistent with that derived for PS1-11bam and LSQ12dlf. Whereas, the M_{ej} estimated for SN 2020ank ($\sim 3.58 \pm 0.04 M_\odot$) is also closer to the M_{ej} obtained for SN 2011kl ($\sim 3.22 \pm 1.47 M_\odot$; Lin et al. 2020). The value of P_i for SN 2020ank is higher whereas B value is lower as compared to those obtained for SN 2011kl ($P_i \sim 0.36$ –0.78 ms and $B \sim (3.1$ –6.8) $\times 10^{14}$ G, respectively, see Bersten et al. 2016; Lin et al. 2020). This is evident in the left panel of the Figure 10 that the GRB associated SN 2011kl shows the highest value of B and lowest value of P_i among all the SLSNe I of the sample (except for SN 2010gx and SN 2013dg).

5 SPECTROSCOPIC ANALYSIS OF SN 2020ank

In this section, we investigate the spectral properties of SN 2020ank using spectral observations taken at six epochs (see section 2 and Table 6). Spectra of SN 2020ank, spanning a duration of about 14 days starting from ~ -1 to $+13$ d (rest frame), are plotted in Figure 11. The phase of each individual spectrum with respect to the g -band maximum (in d) is marked on the right side of each spectrum in respective colours. All the presented spectra are shifted to the rest-frame wavelengths and corrected for the Galactic extinction value of $E(B - V) = 0.023$ mag, whereas the host galaxy extinction was assumed negligible. The publicly available spectra obtained from the GTC-10.4m (at -1.08 d) and the P200-5.1m (at -0.74 d) are shown in cyan, however the spectra observed from the HCT-2.0m (from $+2.98$ to $+13.39$ d) are presented in black. Unfortunately, spectra from the HCT-2.0m have a poor signal to noise ratio. Therefore, these spectra were smoothed using the Savitzky–Golay method by fitting the third-order polynomial function for each λ in the range $\lambda - \lambda/100 < \lambda < \lambda + \lambda/100$ and shown with the magenta colour over-plotted to the HCT-2.0m spectra (see Figure 11). The P200-5.1m spectrum at -0.74 d is also smoothed in the same fashion in the range $\lambda - \lambda/5 < \lambda < \lambda + \lambda/5$, just for the clarity of the spectral features. Details about Savitzky–Golay smoothing technique are described in Quimby et al. (2018).

The near-peak spectrum (at -0.74 d) of SN 2020ank exhibits a bluer continuum, fitted with a BB function having temperature $\sim 14,800 \pm 300$ K. Line identification is done following Pastorello et al. 2010; Yan et al. 2017a; Quimby et al. 2018 and using the spectral fitting codes SYNAPPS and SYN++ (Thomas et al. 2011). The SYNAPPS spectral fitting is attempted for the spectrum at -0.74 d,

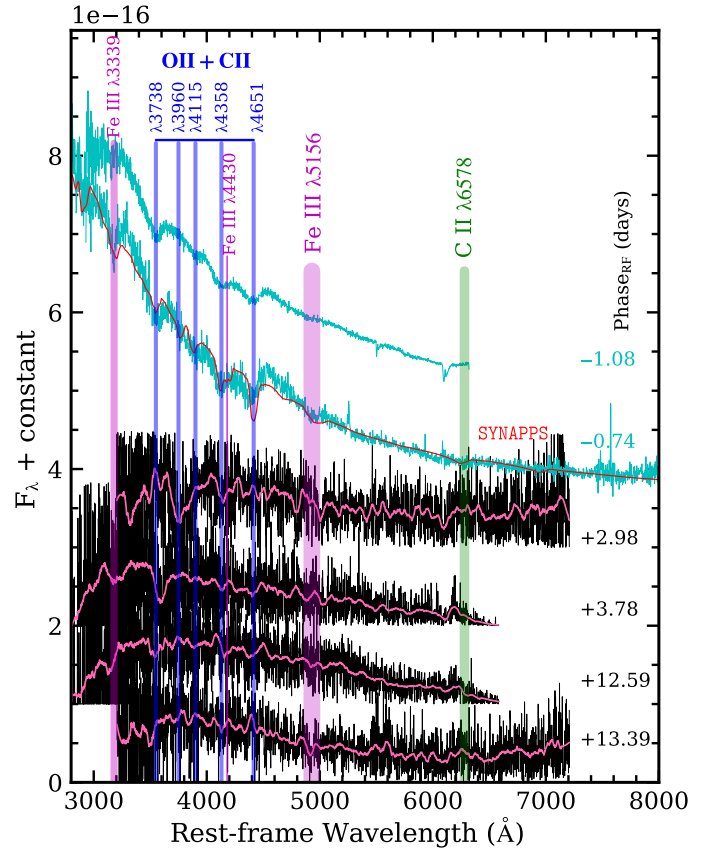


Figure 11. Galactic extinction corrected spectra of SN 2020ank in the rest-frame wavelengths are shown. The phase with respect to the g -band maximum is also mentioned on the right-hand side of each spectrum in their respective colours. The HCT-2.0m spectra are smoothed using the Savitzky–Golay smoothing method (Quimby et al. 2018), and the smoothed spectra are over-plotted with the magenta colour. The near-peak spectrum (at -0.74 d) is regenerated using the SYNAPPS code (Thomas et al. 2011) and shown in the red. The near-peak spectra are dominated by the W-shaped O II features, whereas the weak C II and Fe III lines can also be traced.

and the modelled spectrum is shown with the red colour, see Figure 11, details about the SYNAPPS spectral fitting are discussed in section 5.1. The spectral features are highlighted with the vertical bands at the observed wavelengths, and their respective rest-frame wavelengths are written on the top. The near-peak spectra (at -1.08 and -0.74 d) of SN 2020ank are dominated by the W-shaped O II features ($\lambda 3737.59$, $\lambda 3959.83$, $\lambda 4115.17$, $\lambda 4357.97$ and $\lambda 4650.71$) discussed by Quimby et al. (2018) and exhibiting a clear absence of H and He lines. However, weak signatures of C II ($\lambda 3921$, $\lambda 4267$, $\lambda 6578$ and $\lambda 7234$) and Fe III ($\lambda 3339$, $\lambda 4430$ and $\lambda 5156$) are also traced. In the near-peak spectra, the O II absorption features are highly blue-shifted with respect to their rest-frame wavelengths, indicating an equivalent velocity of $\sim 17,500$ km s^{-1} , and C II ($\lambda 6578$) observed at ~ 6220 Å with a velocity around 16,500 km s^{-1} . On the other hand, Fe III ($\lambda 5156$) observed at ~ 4930 Å, exhibiting a comparatively lower equivalent velocity of $\sim 13,000$ km s^{-1} .

5.1 The SYNAPPS spectral modelling

The parameterized spectrum synthesis code SYNAPPS (Thomas et al. 2011) is a rewritten, automated and improved version of the SYNOW code (written in C++; Fisher 2000; Branch et al. 2002).

Table 6. Log of the spectroscopic observations of SN 2020ank.

Date (UT)	MJD	Phase ^a (d)	Instrument	Wavelength (Å)	Resolution (Å)	Exposure Time (s)	Telescope
2020 Feb 13	58,892.926	−1.084	OSIRIS	3660–7890	2.1	900	GTC-10.4m ^b
2020 Feb 14	58,893.360	−0.737	DBSP	3400–10,500	1.5	500	P200-5.1m ^b
2020 Feb 19	58,898.000	+2.980	HFOC	3500–7800	8	2700	HCT-2.0m
2020 Feb 20	58,899.000	+3.781	HFOC	3500–7800	8	3600	HCT-2.0m
2020 Mar 02	58,910.000	+12.591	HFOC	3500–7800	8	2700	HCT-2.0m
2020 Mar 03	58,911.000	+13.392	HFOC	3500–7800	8	3600	HCT-2.0m

^a Phase is given in the rest-frame d since *g*-band maximum. ^b Downloaded from the TNS; <https://wis-tns.weizmann.ac.il/object/2020ank>.

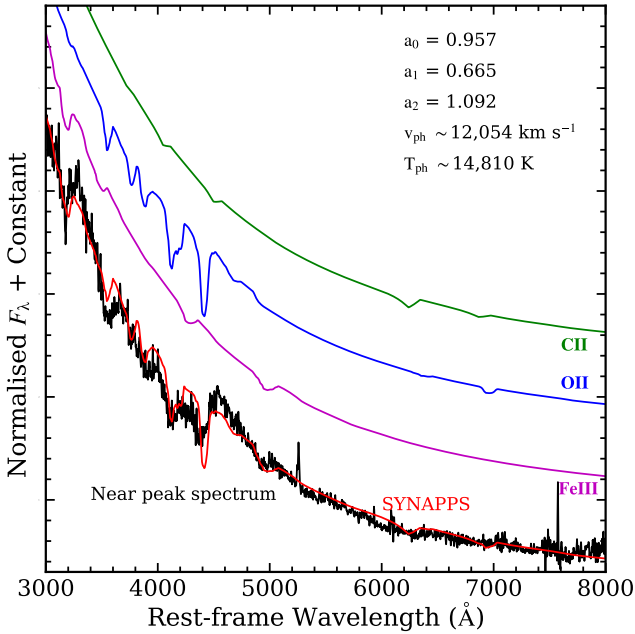


Figure 12. The near-peak spectrum of SN 2020ank and the synthetic spectrum (in red) obtained by the SYNAPPS (Thomas et al. 2011) spectral fitting are shown in the bottom. Individual ion contributions for all the elements that were used to regenerate the best fit spectrum are also shown. All the prominent spectral features are well generated by the code using C II, O II, and Fe III elements. The bluer region (from ~3400 to 4500 Å) of the spectrum is dominated by the W-shaped O II features. The C II and O II features are at higher velocities (~16,500 and 17,750 km s^{−1}, respectively) in comparison to Fe III line velocity (~13,100 km s^{−1}).

The basic assumptions of the code (Thomas et al. 2011) are the following: spherical symmetry, homologous expansion of the ejecta, Sobolev approximation for line formation (Sobolev 1957), and considering the ejecta as a gas with the rapid flow. This code’s limitations are sharp photosphere, BB assumption, and the concept of no electron scattering (Thomas et al. 2011). The code ignores the effects of continuous opacity and deals with local thermodynamic equilibrium (LTE) for maintaining populations at different levels. The SYNAPPS code uses well-structured input known as a YAML file consisting of different global and local parameters. The global parameters are the photospheric velocity (v_{ph}), the outer velocity of the line forming regions (v_{out}), BB photosphere temperature (T_{ph}), and the coefficients of quadratic warping function (a_0 , a_1 , and a_2), which are applied to the synthetic spectrum to match the observed ones. Global parameters decide the overall shape of the spectrum. On the other hand, local parameters like the line opacity (τ), lower

and upper cut off velocities (v_{min} and v_{max} , respectively), aux parameter (aux), and the Boltzmann excitation temperature (T) depend on the individual profiles of the different elements.

In SN ejecta, matter density in shells above the photosphere could be described by two different laws. The first one is the power-law with index “ n ” ($\tau \propto v^{-n}$), which is set for all compositions of ions in the model. The second one is the exponential law with the parameter e-folding velocity “ v_e ” ($\tau \propto \exp(-v/v_e)$), which could be changed for each ion independently. We checked both the cases for our analysis and found that the exponential law is more reliable for fine-tuning. The SYNAPPS code can calculate two shapes of the line profile. The first case corresponds to a layer un-detached from the photosphere, giving rise to conspicuous emission and more gentle sloping to the absorption part of the profile. The second case (detached) describes a layer which has a larger v_{exp} than the photosphere. Therefore, there is a gap between the photosphere and successive layers. In our case, the lines arising due to the O II, C II, and Fe III elements are considered as detached from the photosphere as they exhibit higher velocities in comparison to v_{ph} . In summary, we suppose that the real distribution of matter densities in these layers could enormously differ from the model conceptions but could be used to describe the more conspicuous and dense part of layers.

A better signal to noise ratio of the spectra taken using the GTC-10.4m and P200-5.1m provided an opportunity to perform the SYNAPPS spectral modelling. Consequently, we used the SYNAPPS (Thomas et al. 2011) code to attempt the spectral modelling of the near-peak spectrum (at −0.74 d since *g*-band maximum, whereas ~28.4 d since explosion) of SN 2020ank. We were unable to perform it for the post-peak spectra taken with the HCT-2.0m, because of the poor signal to noise ratio. We also present the contributions from the individual ions to reproduce the near-peak spectrum of SN 2020ank using the SYN++ (Thomas et al. 2011) and the output obtained from the SYNAPPS code, see Figure 12. All the prominent features are well reproduced by the code. The local fitting parameters ($\log \tau$, v_{min} , v_{max} , aux and T) for individual ions obtained from the SYNAPPS spectral fitting are tabulated in Table 7. The global parameters (a_0 , a_1 , a_2 , v_{ph} and T_{ph}) are presented in upper-right side of the Figure 12 itself. The synthetic spectrum is obtained using the C II, O II, and Fe III ions, however, the bluer region (from ~3400 to 4500 Å) is mainly dominated by the W-shaped O II features. The SYNAPPS spectral fitting also shows a clear blending of C II ($\lambda\lambda 3921$ and 4267) and Fe III ($\lambda 4430$) with the O II features in the bluer part of the spectrum. From the best fitted spectrum, a T_{ph} of ~14,810 K and the v_{ph} of ~12,050 km s^{−1} are obtained. It is noteworthy that the estimated v_{ph} is consistent within the error bars with the $v_{exp} \sim 12,270 \pm 900$ km s^{−1} obtained from the bolometric light-curve modelling using the MINIM code (see section 4.1). Also, T_{ph} obtained through the SYNAPPS spectral fitting

Table 7. Best-fit local parameters obtained using the SYNAPPS spectral fitting on the near-peak spectrum of SN 2020ank along with the inferred values of g , $z(T)$, n_l , N and ρ are listed.

Element	$\log \tau$	v_{\min} (10^3 km s^{-1})	v_{\max} (10^3 km s^{-1})	aux	T (10^3 K)	g	$z(T)$	$\log(n_l)$ cm^{-3}	$\log(N)$ cm^{-3}	$\log(\rho)$ g cm^{-3}
C II	-0.773	16.500	47.511	4.068	16.000	6	6.24	3.413	5.902	-16.798
O II	4.554	17.740	31.934	0.651	12.522	—	—	—	—	—
Fe III	2.841	13.110	36.871	0.435	13.234	7	34.48	10.002	12.057	-9.975

($\sim 14,810 \text{ K}$) closely matched to those independently derived using BB fitting to the spectrum ($\sim 14,800 \pm 300 \text{ K}$) and BB fitting to the photometric SED ($\sim 15,400 \pm 800 \text{ K}$) at similar epoch. The absorption minima of lines interpreted as C II and O II were fitted by larger velocities ($\sim 16,500$ and $17,750 \text{ km s}^{-1}$, respectively) than for Fe III ($\sim 13,100 \text{ km s}^{-1}$), see Table 7. However, this spectrum of SN 2020ank could also be modelled using O III and C III in place of O II and C II (Hatano et al. 1999) as suggested by Könyves-Tóth et al. (2020) for the fast-evolving SLSN 2019neq. Using the equations 4 and 6 of Könyves-Tóth et al. (2020), we also estimated the number density of ions at the lower level of the transition (n_l), full number density of the ion (N), and the mass density (ρ , in g cm^{-3}) values for the C II and Fe III ions (see Table 7). To calculate the same, we obtained the statistical weight of the lower level (g) and the partition function ($z(T)$) from the National Institute of Standards and Technology (NIST)⁹ and also tabulated these values in Table 7. The oscillator strength (f) and the excitation potential of the lower level (χ) are adopted from Hatano et al. (1999), whereas values of τ and T are taken from the SYNAPPS spectral fitting. We are unable to calculate the values of n_l , N and ρ for O II ion because the reference line for O II ion is considered as a forbidden transition by Hatano et al. (1999), as also stated by Könyves-Tóth et al. (2020).

Using the estimated v_{ph} from the SYNAPPS spectral fitting and a rise time (t_r , time since date of explosion to the peak bolometric luminosity) of $\sim 27.9 \pm 1.0 \text{ d}$ (rest-frame), we computed photospheric radius (r_{phot}) of $\sim 2.4 \times 10^{15} \text{ cm}$ and total optical depth (τ_{tot}) of ~ 74.6 for SN 2020ank. The details about methods of calculation of the above discussed parameters are well described in Könyves-Tóth et al. (2020). In the case of SN 2020ank, the value of r_{phot} is lower and τ_{tot} is higher in comparison to those estimated for slow-evolving SN 2010kd ($r_{phot} \sim 6.2 \times 10^{15} \text{ cm}$ and $\tau_{tot} \sim 60$) and fast-evolving SN 2019neq ($r_{phot} \sim 5.1 \times 10^{15} \text{ cm}$ and $\tau_{tot} \sim 43$) by Könyves-Tóth et al. (2020). Using the above discussed values of v_{ph} and t_r , we also estimated the M_{ej} ($\sim 7.2 \pm 0.5 M_{\odot}$) and kinetic energy ($E_k \sim (6.3 \pm 0.1) \times 10^{51} \text{ erg}$) for SN 2020ank applying equations 1 and 3 of Wheeler et al. (2015). The estimated value of the E_k for SN 2020ank is nearly 2 to 3 times higher than what neutrino driven explosion can give at maximum and favors a jet feedback mechanism (Soker 2016; Soker & Gilkis 2017). The calculated $M_{ej} \sim 7.2 \pm 0.5 M_{\odot}$ of SN 2020ank (using the spectral analysis) is higher than the M_{ej} obtained from the semi-analytical light curve modelling ($\sim 3.58 \pm 0.04 M_{\odot}$) using the MINIM code (see section 4.1). Comparatively lower value of M_{ej} obtained using the light-curve modelling might attribute to the under-estimation of the peak luminosity by the MAG model. The estimated M_{ej} value of SN 2020ank is lower in comparison to the well studied slow-evolving PTF12dam ($\sim 10 - 16 M_{\odot}$; Nicholl et al. 2013), whereas closer to the fast-evolving SN 2010gx ($\sim 7.1 M_{\odot}$; Inserra et al. 2013).

5.2 Spectral comparison

In the section, we compare the near-peak spectrum of SN 2020ank (in red) with the spectra of SN 2010gx (fast-evolving; Pastorello et al. 2010), PTF12dam (slow-evolving; Nicholl et al. 2013) and Gaia16apd (intermediate-decaying; Kangas et al. 2017; Nicholl et al. 2017a), see Figure 13. Overall, the spectral features of SN 2020ank are similar to the three other SLSNe I. The near-peak spectrum of SN 2020ank appears to closely match with the spectrum of SN 2010gx at -3 d . The closely matched absorption features of SN 2020ank with those of SN 2010gx indicate nearly equal ejecta velocities. The spectral features of SN 2020ank also match well with the -3 d spectrum of Gaia16apd, however, the minima of the absorption features fall at bluer wavelengths, indicating higher ejecta velocity as compared to Gaia16apd. The close spectral resemblance of SN 2020ank with SN 2010gx puts it in the category of “SN 2011ke-like” (fast-evolving) SLSN, as suggested by Quimby et al. (2018). To confirm this fast-spectral evolution, we compare the near-peak spectrum of SN 2020ank with the near- and post-peak spectra (at $+22 \text{ d}$) of PTF12dam (slow-evolving). The near peak spectral features of SN 2020ank appear similar to that were observed in the spectrum of PTF12dam at $+22 \text{ d}$, confirming the comparatively faster spectral evolution of SN 2020ank.

6 RESULTS AND CONCLUSION

We have presented the early optical photometric and spectroscopic observations of the fast-evolving and bright SLSN 2020ank. The photometric data were obtained in the Bessell U , B , V , R , and I bands (from $\sim +3$ to $+52 \text{ d}$, rest-frame) using the ST-1.04m, HCT-2.0m, and the DOT-3.6m along with the publicly available SDSS g and r bands data (from ~ -21 to $+36 \text{ d}$, rest-frame) from the ZTF. The spectral analysis were performed on the post-peak spectra observed with the HCT-2.0m (from $\sim +3$ to $+13 \text{ d}$, rest-frame) at four epochs. These spectral data were also supplemented by two publicly available spectra obtained from the GTC-10.4m and the P200-5.1m (at -1.08 and -0.74 d , rest-frame). Apart from providing well-calibrated photometric data of this newly discovered bright and fast-evolving SLSN, the main findings of the present analysis are the following:

1) The post-peak decay rate of SN 2020ank in the rest-frame U -band is consistent with the theoretical decay rate of $^{56}\text{Ni} \rightarrow ^{56}\text{Co}$ (0.11 mag d^{-1}) and turns shallower as we go towards redder bands ($\sim 0.05 \text{ mag d}^{-1}$ for R -band). Also, the light curve decay of SN 2020ank seems steeper than other well-studied slow-decaying SLSNe I.

2) The well-sampled rest-frame g -band light-curve exhibits a peak-absolute magnitude of $\sim -21.84 \pm 0.10 \text{ mag}$, indicating SN 2020ank as one of the bright SLSNe I. The pre-peak rising and post-peak decaying rates of the light curve are similar to other well-studied fast-evolving SLSNe I (e.g., SN 2010gx, PTF11rks, and

⁹ <https://www.nist.gov/pml/atomic-spectra-database>

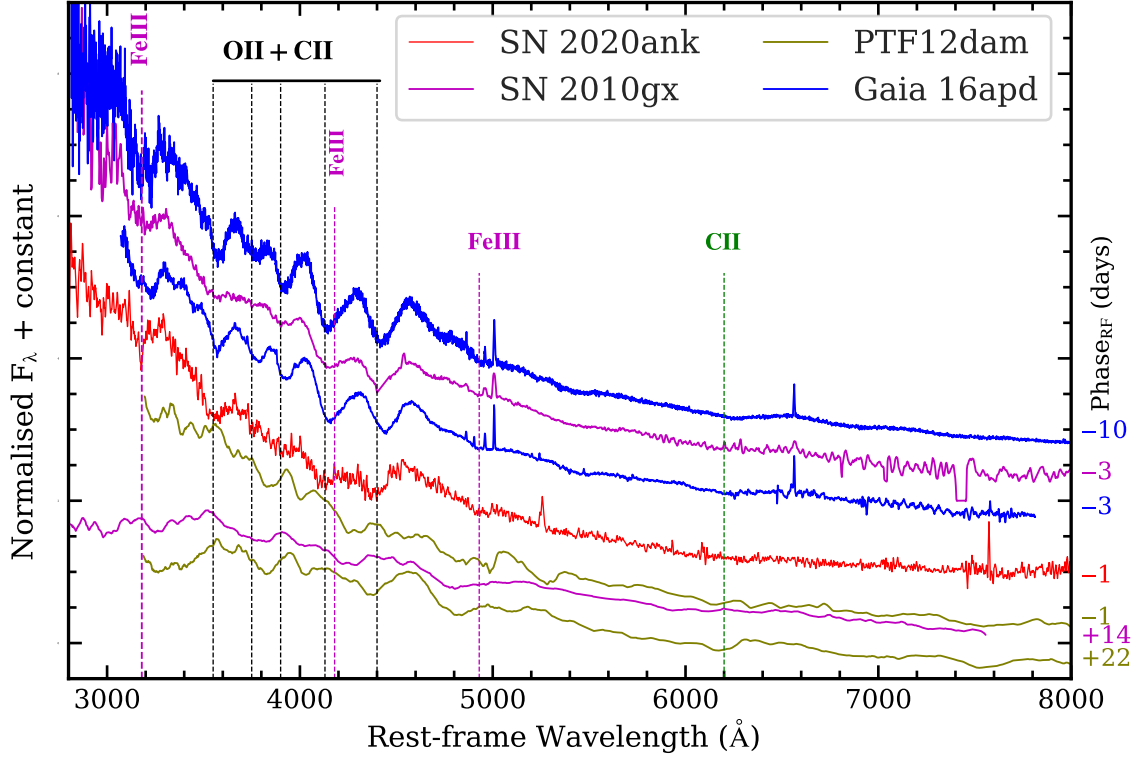


Figure 13. The near-peak spectrum of SN 2020ank (in red) is compared with some of the well studied SLSNe I: SN 2010gx (in magenta; Pastorello et al. 2010), PTF12dam (in olive; Nicholl et al. 2013) and Gaia16apd (in blue; Kangas et al. 2017; Nicholl et al. 2017a). The spectral features of SN 2020ank are apparently match with those observed in the case of SN 2010gx suggesting it as yet another fast-evolving SLSN.

SN 2011ke) but comparatively steeper in comparison to the slow-evolving SLSNe I (e.g., SN 2010kd, PTF12dam, and SN 2015bn). However, the rest-frame $g - r$ colour evolution of SN 2020ank is not consistent with the fast-evolving SLSNe I and is closer to the slow-evolving ones.

3) The bolometric light-curve of SN 2020ank is symmetric around the peak with $L_{\text{max}}^{\text{rise}}/e \approx L_{\text{max}}^{\text{fall}}/e \approx 15$ d and takes nearly 27 d to reach the L_{max} of $\sim 4 \times 10^{44}$ erg s $^{-1}$. The estimated value of the L_{max} for SN 2020ank is higher than SN 2010gx, SN 2010kd, PTF12dam, SN 2015bn, Gaia16apd, etc., whereas lower in comparison to that were observed for SN 2011ke, PTF13ajg, and ASASSN-15lh. Overall, the light-curve comparison of SN 2020ank with other well-studied slow- and fast-evolving SLSNe I suggests that it is a fast-evolving SLSN having a high peak brightness.

4) Semi-analytical light-curve modelling using MINIM rules out radioactive decay and the CSMI as possible powering mechanisms for SN 2020ank. Our findings suggest a spin-down millisecond magnetar having P_i of $\sim 2.23 \pm 0.51$ ms and $B \sim (2.91 \pm 0.07) \times 10^{14}$ G as possibly powering source with total ejected mass of $\sim 3.58 \pm 0.04 M_{\odot}$. The observed excess UV flux near the peak in the case of SN 2020ank also supports the central engine based power source.

5) Spectroscopic analysis helped to probe chemical composition of the ejecta and constrain crucial physical parameters of SN 2020ank. The SYNAPPS spectral modelling reveals that the near-peak spectrum of SN 2020ank is dominated by the W-shaped O II features along with comparatively fewer contributions from the C II and Fe III species. The T_{ph} ($\sim 14,800$ K) and v_{ph} ($\sim 12,050$ km s $^{-1}$) estimated by the SYNAPPS code are consistent within error bars to the T_{BB} calculated from SED fitting to the photometric data

($\sim 15,400 \pm 800$ K) and v_{exp} ($\sim 12,270 \pm 900$ km s $^{-1}$) computed by the best fitted MAG model.

6) Using the value of v_{ph} obtained from the SYNAPPS spectral fitting and assuming diffusion timescale $\approx t_r$ ($\sim 27.9 \pm 1.0$ d) with $\kappa = 0.1$ cm 2 g $^{-1}$, we constrain the r_{phot} ($\sim 2.4 \times 10^{15}$ cm), τ_{tot} (~ 74.6), M_{ej} ($\sim 7.2 M_{\odot}$) and E_k ($\sim 6.3 \times 10^{51}$ erg) for SN 2020ank.

7) The near-peak spectral comparison of SN 2020ank shows that the spectral features are similar to those observed in SN 2010gx and Gaia16apd. However, higher blue-shifted absorption features in SN 2020ank than Gaia16apd indicate higher ejecta velocity in the former. The near-peak spectral similarity with SN 2010gx and apparent similarity with the spectrum of the PTF12dam (slow-evolving) at +22 d confirms comparatively faster spectral evolution of SN 2020ank.

ACKNOWLEDGEMENTS

This study uses the data from the ST-1.04m, HCT-2.0m, and DOT-3.6m, and authors of this paper are highly thankful to the observing staff and observing assistants for their support during observations of SN 2020ank in the trying times of the CoVID-19 pandemic. AK and SBP acknowledge the guidance and discussions related to the physics of core-collapse Supernovae with Prof. J. Craig Wheeler and Prof. Jozsef Vinkó. AK would also like to thank Prof. Matt Nicholl, Raya Dastidar and Kaushal Sharma for the insightful discussion. This study also uses the publicly available photometric data of the Samuel Oschin 48-inch Telescope at the Palomar Observatory as part of the ZTF project. ZTF is supported by the National Science Foundation under Grant

No. AST-1440341 and a collaboration including Caltech, IPAC, the Weizmann Institute for Science, the Oskar Klein Center at Stockholm University, the University of Maryland, the University of Washington, Deutsches Elektronen-Synchrotron and Humboldt University, Los Alamos National Laboratories, the TANGO Consortium of Taiwan, the University of Wisconsin at Milwaukee and Lawrence Berkeley National Laboratories. Operations are conducted by COO, IPAC, and UW. We used the publicly available spectrum of SN 2020ank based on observations made with the GTC-10.4m, installed at the Spanish Observatorio del Roque de los Muchachos of the Instituto de Astrofísica de Canarias, in the island of La Palma. This study also used the publicly available spectrum of P200 Hale telescope. S.B.P., K.M., A.A., and R.G. acknowledge BRICS grant DST/IMRCD/BRICS/Pilotcall/ProFCheap/2017(G) and DST/JSPS grant DST/INT/JSPS/P/281/2018 for this work. This research has utilized the NED, which is operated by the Jet Propulsion Laboratory, California Institute of Technology, under contract with NASA. We acknowledge the use of NASA's Astrophysics Data System Bibliographic Services. This research also made use of the Open Supernova Catalog (OSC) currently maintained by James Guillochon and Jerod Parrent.

DATA AVAILABILITY

The photometric and spectroscopic data used in this work can be made available on request to the corresponding author.

REFERENCES

- Angus C. R., et al., 2019, *MNRAS*, **487**, 2215
- Bellm E. C., et al., 2019, *PASP*, **131**, 018002
- Bersten M. C., Benvenuto O. G., Orellana M., Nomoto K., 2016, *ApJ*, **817**, L8
- Blanchard P. K., et al., 2018, *ApJ*, **865**, 9
- Bose S., et al., 2018, *ApJ*, **853**, 57
- Brachetti P., Felice Ciccoli M., di Pillo G., Lucidi S., 1997, *Journal of Global Optimization*, **10**, 165
- Branch D., Wheeler J. C., 2017, *Supernova Explosions*, doi:10.1007/978-3-662-55054-0.
- Branch D., et al., 2002, *ApJ*, **566**, 1005
- Breeveld A. A., Landsman W., Holland S. T., Roming P., Kuin N. P. M., Page M. J., 2011, in McEnery J. E., Racusin J. L., Gehrels N., eds, *American Institute of Physics Conference Series Vol. 1358, Gamma Ray Bursts 2010*. pp 373–376 (arXiv:1102.4717), doi:10.1063/1.3621807
- Chatzopoulos E., Tuminello R., 2019, *ApJ*, **874**, 68
- Chatzopoulos E., et al., 2011, *ApJ*, **729**, 143
- Chatzopoulos E., Wheeler J. C., Vinko J., 2012, *ApJ*, **746**, 121
- Chatzopoulos E., Wheeler J. C., Vinko J., Horvath Z. L., Nagy A., 2013, *ApJ*, **773**, 76
- Chen T. W., et al., 2015, *MNRAS*, **452**, 1567
- Chen T.-W., Smartt S. J., Yates R. M., Nicholl M., Krühler T., Schady P., Dennefeld M., Inserra C., 2017a, *MNRAS*, **470**, 3566
- Chen T. W., et al., 2017b, *A&A*, **602**, A9
- Chornock R., et al., 2013, *ApJ*, **767**, 162
- Dahiwalé A., Fremling C., 2020, *Transient Name Server Classification Report*, 2020-1494, 1
- De Cia A., et al., 2018, *ApJ*, **860**, 100
- Denneau L., 2014, in Wozniak P. R., Graham M. J., Mahabal A. A., Seaman R., eds, *The Third Hot-wiring the Transient Universe Workshop*. pp 65–65
- Dessart L., 2019, *A&A*, **621**, A141
- Dessart L., Hillier D. J., Waldman R., Livne E., Blondin S., 2012, *MNRAS*, **426**, L76
- Dong S., et al., 2016, *Science*, **351**, 257
- Fisher A. K., 2000, PhD thesis, THE UNIVERSITY OF OKLAHOMA
- Gal-Yam A., 2012, *Science*, **337**, 927
- Gal-Yam A., 2019a, *ARA&A*, **57**, 305
- Gal-Yam A., 2019b, *ApJ*, **882**, 102
- Gal-Yam A., et al., 2009, *Nature*, **462**, 624
- Gezari S., et al., 2009, *ApJ*, **690**, 1313
- Ginzburg S., Balberg S., 2012, *ApJ*, **757**, 178
- Gomez S., Berger E., Blanchard P. K., Hosseinzadeh G., Nicholl M., Villar V. A., Yin Y., 2020, *ApJ*, **904**, 74
- Greiner J., et al., 2015, *Nature*, **523**, 189
- Hatano K., Branch D., Fisher A., Millard J., Baron E., 1999, *ApJS*, **121**, 233
- Hogg D. W., Baldry I. K., Blanton M. R., Eisenstein D. J., 2002, arXiv e-prints, pp astro-ph/0210394
- Inserra C., 2019, *Nature Astronomy*, **3**, 697
- Inserra C., et al., 2013, *ApJ*, **770**, 128
- Inserra C., et al., 2017, *MNRAS*, **468**, 4642
- Inserra C., et al., 2018a, *MNRAS*, **475**, 1046
- Inserra C., et al., 2018b, *A&A*, **609**, A83
- Inserra C., Prajs S., Gutierrez C. P., Angus C., Smith M., Sullivan M., 2018c, *ApJ*, **854**, 175
- Janka H.-T., 2012, *Annual Review of Nuclear and Particle Science*, **62**, 407
- Jerkstrand A., et al., 2017, *ApJ*, **835**, 13
- Jordi K., Grebel E. K., Ammon K., 2006, *A&A*, **460**, 339
- Kangas T., et al., 2017, *MNRAS*, **469**, 1246
- Kann D. A., et al., 2019, *A&A*, **624**, A143
- Kasen D., Bildsten L., 2010, *ApJ*, **717**, 245
- Kasen D., Woosley S. E., Heger A., 2011, *ApJ*, **734**, 102
- Könyves-Tóth R., Vinkó J., 2020, arXiv e-prints, p. arXiv:2011.00883
- Könyves-Tóth R., Thomas B. P., Vinkó J., Wheeler J. C., 2020, *ApJ*, **900**, 73
- Kozyreva A., Blinnikov S., 2015, *MNRAS*, **454**, 4357
- Kumar B., Singh A., Srivastav S., Sahu D. K., Anupama G. C., 2018, *MNRAS*, **473**, 3776
- Kumar A., et al., 2020, *ApJ*, **892**, 28
- Landolt A. U., 1992, *AJ*, **104**, 340
- Lee C.-H., 2020, *Astronomische Nachrichten*, **341**, 651
- Leloudas G., et al., 2012, *A&A*, **541**, A129
- Leloudas G., et al., 2015, *MNRAS*, **449**, 917
- Lin J., Lu R.-J., Lin D.-B., Wang X.-G., 2020, *ApJ*, **895**, 46
- Liu L.-D., Wang S.-Q., Wang L.-J., Dai Z.-G., Yu H., Peng Z.-K., 2017a, *ApJ*, **842**, 26
- Liu Y.-Q., Modjaz M., Bianco F. B., 2017b, *ApJ*, **845**, 85
- Lunnan R., et al., 2014, *ApJ*, **787**, 138
- MacFadyen A. I., Woosley S. E., 1999, *ApJ*, **524**, 262
- Mazzali P. A., Sullivan M., Pian E., Greiner J., Kann D. A., 2016, *MNRAS*, **458**, 3455
- McCrum M., et al., 2015, *MNRAS*, **448**, 1206
- Metzger B. D., Margalit B., Kasen D., Quataert E., 2015, *MNRAS*, **454**, 3311
- Miller A. A., et al., 2009, *ApJ*, **690**, 1303
- Mohan V., Uddin W., Sagar R., Gupta S. K., 1999, *Bulletin of the Astronomical Society of India*, **27**, 601
- Moré J. J., 1978, *The Levenberg-Marquardt algorithm: Implementation and theory*. pp 105–116, doi:10.1007/BFb0067700
- Moriya T. J., Sorokina E. I., Chevalier R. A., 2018, *Space Sci. Rev.*, **214**, 59
- Nagy A. P., 2018, *ApJ*, **862**, 143
- Nicholl M., 2018, *Research Notes of the American Astronomical Society*, **2**, 230
- Nicholl M., et al., 2013, *Nature*, **502**, 346
- Nicholl M., et al., 2014, *MNRAS*, **444**, 2096
- Nicholl M., et al., 2015a, *MNRAS*, **452**, 3869
- Nicholl M., et al., 2015b, *ApJ*, **807**, L18
- Nicholl M., et al., 2016, *ApJ*, **826**, 39
- Nicholl M., Berger E., Margutti R., Blanchard P. K., Milisavljevic D., Chalis P., Metzger B. D., Chornock R., 2017a, *ApJ*, **835**, L8
- Nicholl M., Guillochon J., Berger E., 2017b, *ApJ*, **850**, 55

- Nicholl M., Berger E., Blanchard P. K., Gomez S., Chornock R., 2019, *ApJ*, **871**, 102
- Osterbrock D. E., 1989, *Astrophysics of gaseous nebulae and active galactic nuclei*
- Pandey S. B., 2016, in *Revista Mexicana de Astronomia y Astrofisica Conference Series*. pp 83–88
- Pandey S. B., 2018, in *SN 1987A, Quark Phase Transition in Compact Objects and Multimessenger Astronomy*. pp 149–157, doi:10.26119/SAO.2020.1.52328
- Pandey S. B., Yadav R. K. S., Nanjappa N. i., Yadav S., Reddy B. K., Sahu S., Srinivasan R., 2018, *Bulletin de la Societe Royale des Sciences de Liege*, **87**, 42
- Pastorello A., et al., 2010, *ApJ*, **724**, L16
- Perley D. A., et al., 2016, *ApJ*, **830**, 13
- Piro A. L., 2015, *ApJ*, **808**, L51
- Poidevin F., et al., 2020a, *The Astronomer’s Telegram*, **13489**, 1
- Poidevin F., et al., 2020b, *Transient Name Server Discovery Report*, **2020-234**, 1
- Poznanski D., Prochaska J. X., Bloom J. S., 2012, *MNRAS*, **426**, 1465
- Prajs S., et al., 2017, *MNRAS*, **464**, 3568
- Pursiainen M., et al., 2018, *MNRAS*, **481**, 894
- Quimby R. M., Aldering G., Wheeler J. C., Höflich P., Akerlof C. W., Rykoff E. S., 2007, *ApJ*, **668**, L99
- Quimby R. M., et al., 2011, *Nature*, **474**, 487
- Quimby R. M., Yuan F., Akerlof C., Wheeler J. C., 2013, *MNRAS*, **431**, 912
- Quimby R. M., et al., 2018, *ApJ*, **855**, 2
- Schlafly E. F., Finkbeiner D. P., 2011, *ApJ*, **737**, 103
- Schulze S., et al., 2018, *MNRAS*, **473**, 1258
- Smith M., et al., 2016, *ApJ*, **818**, L8
- Smith K. W., et al., 2019, *Research Notes of the American Astronomical Society*, **3**, 26
- Sobolev V. V., 1957, *Soviet Ast.*, **1**, 678
- Soker N., 2016, *New Astron.*, **47**, 88
- Soker N., Gilkis A., 2017, *ApJ*, **851**, 95
- Stetson P. B., 1987, *PASP*, **99**, 191
- Stetson P. B., 1992, in Worrall D. M., Biemesderfer C., Barnes J., eds, *Astronomical Society of the Pacific Conference Series Vol. 25, Astronomical Data Analysis Software and Systems I*. p. 297
- Taddia F., et al., 2018, *A&A*, **609**, A136
- Thomas R. C., Nugent P. E., Meza J. C., 2011, *PASP*, **123**, 237
- Tonry J., et al., 2020, *Transient Name Server Discovery Report*, **2020-279**, 1
- Umeda H., Nomoto K., 2002, *ApJ*, **565**, 385
- Umeda H., Nomoto K., 2008, *ApJ*, **673**, 1014
- Vreeswijk P. M., et al., 2014, *ApJ*, **797**, 24
- Vreeswijk P. M., et al., 2017, *ApJ*, **835**, 58
- Wang S.-Q., Wang L.-J., Dai Z.-G., 2019, *Research in Astronomy and Astrophysics*, **19**, 063
- Wheeler J. C., Johnson V., Clocchiatti A., 2015, *MNRAS*, **450**, 1295
- Wheeler J. C., Chatzopoulos E., Vinkó J., Tuminello R., 2017, *ApJ*, **851**, L14
- Woosley S. E., 2010, *ApJ*, **719**, L204
- Yan L., et al., 2015, *ApJ*, **814**, 108
- Yan L., et al., 2017a, *ApJ*, **840**, 57
- Yan L., et al., 2017b, *ApJ*, **848**, 6